



Cryo-EM structure of an extracellular *Geobacter* OmcE cytochrome filament reveals tetrahaem packing

Fengbin Wang^{1,7}, Khawla Mustafa^{2,7}, Victor Suci³, Komal Joshi⁴, Chi H. Chan⁴, Sol Choi⁴, Zhangli Su⁵, Dong Si³, Allon I. Hochbaum^{2,6}✉, Edward H. Egelman¹✉ and Daniel R. Bond⁴✉

Electrically conductive appendages from the anaerobic bacterium *Geobacter sulfurreducens* were first observed two decades ago, with genetic and biochemical data suggesting that conductive fibres were type IV pili. Recently, an extracellular conductive filament of *G. sulfurreducens* was found to contain polymerized c-type cytochrome OmcS subunits, not pilin subunits. Here we report that *G. sulfurreducens* also produces a second, thinner appendage comprised of cytochrome OmcE subunits and solve its structure using cryo-electron microscopy at ~4.3 Å resolution. Although OmcE and OmcS subunits have no overall sequence or structural similarities, upon polymerization both form filaments that share a conserved haem packing arrangement in which haems are coordinated by histidines in adjacent subunits. Unlike OmcS filaments, OmcE filaments are highly glycosylated. In extracellular fractions from *G. sulfurreducens*, we detected type IV pili comprising PilA-N and -C chains, along with abundant B-DNA. OmcE is the second cytochrome filament to be characterized using structural and biophysical methods. We propose that there is a broad class of conductive bacterial appendages with conserved haem packing (rather than sequence homology) that enable long-distance electron transport to chemicals or other microbial cells.

Dissimilatory metal-reducing bacterial species such as *Geobacter* are capable of a highly flexible mode of anaerobic respiration in which environmental metal oxides and insoluble electron acceptors outside of the bacterial cell serve as the sole electron acceptors. These electrogenic organisms can transmit electrons to extracellular Fe(III), Mn(IV), U(VI)¹, Tc(VII)², V(V)³, high-molecular-weight humic substances⁴, electrodes⁵ and directly to other cells^{6,7} via a complex series of redox proteins that include conductive filamentous appendages⁸. While *Geobacter* spp. are central to natural and technological processes such as metal cycling⁹, subsurface remediation^{10–12}, waste treatment¹³ and emerging energy generation applications^{14–17}, the identity and bioelectronic properties of the extracellular conductive biomolecules enabling these technologies remain a topic of active debate.

The multihaem c-type cytochromes OmcE, OmcS and OmcZ are typically the most abundant proteins sheared from the *G. sulfurreducens* cell surface after growth with metal oxides or electrode surfaces, and mutants lacking these cytochromes are defective in many aspects of extracellular electron transfer^{18,19}. However, previous studies concluded that such cytochromes are unnecessary for *G. sulfurreducens* long-range extracellular conductivity, based on the hypothesis that *Geobacter* also possesses conductive non-haem 'nanowires'. These appendages, referred to as 'e-pili', are proposed to be built entirely from the N-terminal chain of the type IV pilin, PilA-N, and to be capable of metallic-like conductivity due to electronic coupling between aromatic amino acids^{20–24}.

Recent findings suggest a more complex model of extracellular structures produced by *G. sulfurreducens*. Cryo-electron microscopy (cryo-EM) reconstructions at near-atomic resolution show that OmcS forms filaments containing a haem core^{25,26} and that these filaments are conductive²⁶, while scanning probe imaging and spectroscopy data suggest that OmcZ polymerizes into a distinct filament²⁷. The type IV pilus of *G. sulfurreducens* is a non-conductive filament found in extracellular preparations. This pilus is composed of two chains (PilA-N and PilA-C) lacking the closely spaced aromatic residues that were originally proposed to support long-range electron transport in the PilA-N-only pilus model²⁸. Consistent with the presence of cytochrome appendages, energy-dispersive X-ray spectroscopy imaging also found iron-rich fibres extending from *G. sulfurreducens* cells²⁹. Based on these data, a more exhaustive structural analysis of extracellular conductive filaments is warranted³⁰. To date, the only atomic structure of an extracellular cytochrome filament^{25,26} reported is for the OmcS cytochrome.

While biochemical and structural data are available for OmcS, OmcE has proved more difficult to characterize despite evidence that it plays a crucial role in extracellular respiration. *G. sulfurreducens* mutants lacking *omcE* (GSU0618) are defective in reduction of Fe(III) oxides, Mn(IV) oxides¹⁸, electrodes^{31,32}, U(VI)³³ and humic acids³⁴. *G. metallireducens omcE* (Gmet_2896) mutants are also defective in Fe(III) oxide³⁵ and riboflavin reduction³⁶. During 'direct interspecies electron transfer', when *G. metallireducens* respire by transmitting electrons to *G. sulfurreducens*, *G. metallireducens omcE* is essential but can be partially replaced by the addition of

¹Department of Biochemistry and Molecular Genetics, University of Virginia School of Medicine, Charlottesville, VA, USA. ²Department of Chemistry, University of California, Irvine, Irvine, CA, USA. ³Division of Computing and Software Systems, University of Washington Bothell, Bothell, WA, USA.

⁴Department of Plant and Microbial Biology and BioTechnology Institute, University of Minnesota, Saint Paul, MN, USA. ⁵Department of Genetics, University of Alabama at Birmingham, Birmingham, AL, USA. ⁶Department of Materials Science and Engineering, Department of Molecular Biology and Biochemistry and Department of Chemical and Biomolecular Engineering, University of California, Irvine, Irvine, CA, USA. ⁷These authors contributed equally: Fengbin Wang, Khawla Mustafa. ✉e-mail: hochbaum@uci.edu; egelman@virginia.edu; dbond@umn.edu

conductive minerals^{13,36–38}. Transcriptional data also indicate the involvement of OmcE in extracellular conductivity, because *G. sulfurreducens* expression of *omcE* increased threefold with Fe(III) oxides and as much as ninefold with electrodes compared with growth using soluble electron acceptors^{19,31,39}. Growth of *G. metallireducens* with Fe(III) oxides also upregulated *omcE* 4.4-fold³⁵ and, in the absence of an abiotic conductive medium to aid direct electron transfer to *G. sulfurreducens*, *G. metallireducens omcE* expression increased ninefold³⁸.

The study of extracellular filaments, and their roles, in *Geobacter* spp. is challenging owing to the complex regulatory relationships between type IV pili and extracellular cytochrome production. Deletion of the *pilA-N* gene (GSU1497) or other outer membrane proteins affects which cytochromes and filaments are produced by *Geobacter*^{37,40–42}. Mutations within *pilA-N* alter the ratios of extracellular OmcS and OmcZ, which changes the measured conductivity of extracellular filament preparations^{27,43,44}. These effects suggest that some cytochromes might interact with pili²⁸ similar to how *Francisella*⁴⁵, *Vibrio*⁴⁶, *Dichelobacter*⁴⁷ and *Escherichia coli*⁴⁸ use a type IV pilus biogenesis system for secretion of virulence factors. Because the expression of *omcS* and *omcZ* is influenced by the PilS/PilR two-component regulatory system and intracellular cyclic dinucleotide pools, both of which can be affected by PilA levels^{23,49,50}, manipulation of *pilA* or *omcS* often results in unexpected changes in extracellular cytochrome levels^{23,51}.

In this work we determine the unstudied OmcE cytochrome structure by cryo-EM. We constructed *G. sulfurreducens* strains containing three different *omcS* mutations that were intended to alter the electronic structure of haem chains within OmcS, but a serendipitous outcome was that these *omcS* mutations resulted in an enrichment of extracellular OmcE filaments.

Results

Detection of OmcE in extracellular preparations. To study the details of charge transport within OmcS filaments, we made mutations that would perturb electron transport along the haem core. We engineered three *G. sulfurreducens* strains that each expressed a different single OmcS variant altering a histidine coordinating a haem within OmcS (H357M, H41M and H38M)³². Both H357 and H41 coordinate the same haem in OmcS, while H38 coordinates a different haem. After shearing of proteins from cells and recovery by ammonium sulfate precipitation as previously described²⁶, OmcS or OmcS-like filaments (see below) were observed as bundles and aggregates, along with a mixture of other fibres. Strikingly, after centrifugation at 8,000g for 30 min and treatment with DNase I, the only structures observed using cryo-EM were thinner than OmcS and represented a previously uncharacterized cytochrome filament (Fig. 1 and Extended Data Fig. 1). This suggested to us that cells were compensating for a partial or complete loss of function in OmcS by expressing a different cytochrome filament.

Cryo-EM of the OmcE filament. To characterize these thin filaments we used cryo-EM (Fig. 1a) and determined the structure to 4.3 Å resolution. An averaged power spectrum from raw segments (Extended Data Fig. 2) showed a meridional layer line at $\sim 1/(34 \text{ Å})$, corresponding to the rise per subunit in the filament, and another layer line near the equator at $\sim 1/(207 \text{ Å})$ corresponding to the 207 Å pitch of a one-start helix. These observations provided the initial helical parameters used to generate a $\sim 4.3\text{-Å}$ -resolution reconstruction as judged by Map:Map Fourier shell correlation (FSC). The Model:Map FSC (using the model generated below) gave a similar resolution estimation (Extended Data Fig. 3 and Supplementary Table 1). The filament differed from OmcS in both size and morphology, with a rise per subunit of $\sim 34 \text{ Å}$ with 6.1 subunits per turn (a twist of $\sim 59^\circ$) (Extended Data Fig. 2) compared with the 46.7 Å rise per subunit and 4.3 subunits per turn of OmcS.

These filaments did not show as clear a sinusoidal morphology as OmcS filaments. Filaments were $\sim 40 \text{ Å}$ at their widest point compared with the $\sim 50 \text{ Å}$ of OmcS, and the density map clearly showed that they contained four haems per subunit as compared with six per OmcS subunit.

OmcE fit into the cryo-EM map with a real-space correlation coefficient (RSCC) of 0.7 (Extended Data Fig. 5). To test the hypothesis that the filament was OmcE, we used AlphaFold2 to compare predicted structures for all eight tetrahaem proteins encoded in the *G. sulfurreducens* genome against the experimentally determined density map. Highly accurate protein structure prediction is now possible with AlphaFold2, even if the protein of interest has minimal sequence identity or similarity with proteins of known structure⁵³. Four tetrahaem cytochromes had very different folds and were excluded (Extended Data Fig. 4a,b) as being potential subunits in the filament. The remaining four cytochromes (OmcE, OmcP, GSU1787 and GSU3221) roughly matched the dimensions of the subunit in the map, and were investigated further.

Of these four cytochromes, only OmcE has eight histidine residues near the Fe densities to assemble bis-coordinated haems (Extended Data Fig. 4) and was determined to be the correct protein, with a much higher real-space correlation coefficient compared with the second-best fit protein, which was OmcP (0.70 versus 0.35).

Using mass spectrometry analysis, we confirmed that the thin filament was OmcE by showing that OmcE, but not OmcP, was present in the samples used to obtain the cryo-EM map (Extended Data Fig. 5). Consistent with this conclusion, others have reported transcriptional data showing that *omcE* expression levels are tenfold higher than *omcP* or GSU1787 (ref. 54) under the conditions we used to obtain filaments. Furthermore, *omcE* also had a similar operon structure to the nanowire *omcS*, with an NHL-domain protein upstream of the cytochrome and no lipoproteins or accessory cytochromes to suggest that it was part of an integral membrane porin-cytochrome complex^{18,55}. GSU1787 and GSU3221 cytochromes were detected in our mass spectroscopy data, which suggests that they either exist in a non-filamentous form in the isolates or that they form filaments that are of far lower abundance and therefore remain undetected in the cryo-EM image analyses.

Sequence and structural comparison of OmcE and OmcS.

Because OmcE filaments are only the second experimentally determined cytochrome appendage atomic structure, our next question was whether OmcE shares any sequence or structural homology with OmcS. At the sequence level, OmcE had no detectable homology to OmcS, with $\sim 10\%$ sequence identity (Extended Data Fig. 6). Alignment of their cryo-EM three-dimensional (3D) structures also suggested no similarities in the fold, although both proteins are mainly composed of random coil domains (OmcE has $\sim 3\%$ of residues in β -strands and $\sim 17\%$ in helices, leaving $\sim 80\%$ in coils and turns). The haems in OmcE are bis-His coordinated, as are those in OmcS (Fig. 1c,d). The minimum edge-to-edge distances between haems are also similar, ranging from 3.5 to 4.0 Å, suggesting similar electron transport behaviours in OmcE and OmcS filaments, and both structures have one interfacial haem per subunit coordinated by histidine ligands from an adjacent subunit.

Closer inspection of the quasi-one-dimensional arrangement of the haem chains along the filament core in OmcE and OmcS filaments revealed a further similarity. Despite the lack of overall backbone structural homology between the two proteins, the positions of the four haems in OmcE, as well as their coordinating histidines, aligned with the first four haems of OmcS (Fig. 2c). While the sequence similarity between both cytochromes was low, 28 atom pairs could be aligned between OmcE (200 residues) and OmcS (406 residues), with a root mean squared deviation (RMSD) of $\sim 1.1 \text{ Å}$. When comparing atom pairs across most of the OmcE model,

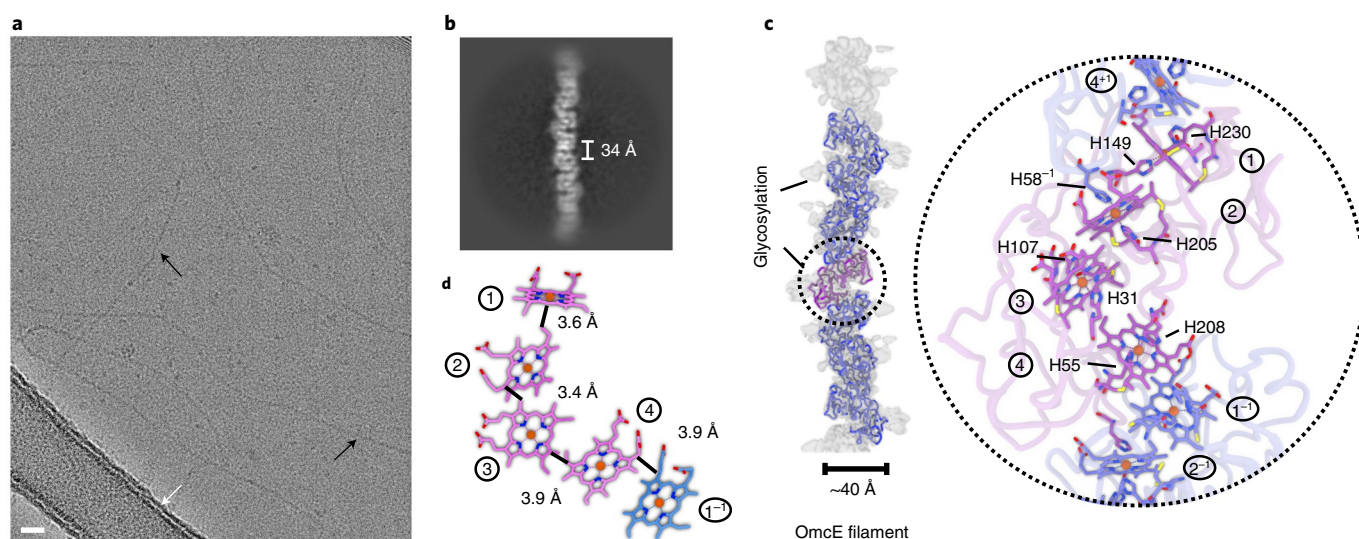


Fig. 1 | Cryo-EM of OmcE filaments. **a**, Representative cryo-EM image of purified OmcE filaments (black arrows) from the OmcS-H357M-producing variant strain of *G. sulfurreducens*, taken from the 35,976 images recorded. Lacey carbon grids were used for cryo-EM imaging (carbon film indicated by white arrow). The sample was treated with DNase I before freezing. Scale bar, 200 Å. **b**, 2D class average of the OmcE filament, showing the increase of 34 Å between adjacent subunits. **c**, The surface of the reconstruction (transparent grey) with backbone trace of the OmcE subunits. A zoomed-in region of the circle is shown on the right, with haems and their coordinating histidines labelled. **d**, The haem array in OmcE, with the minimum observed edge-to-edge distances indicated between adjacent haems. The haem from the adjacent subunit is shown in blue.

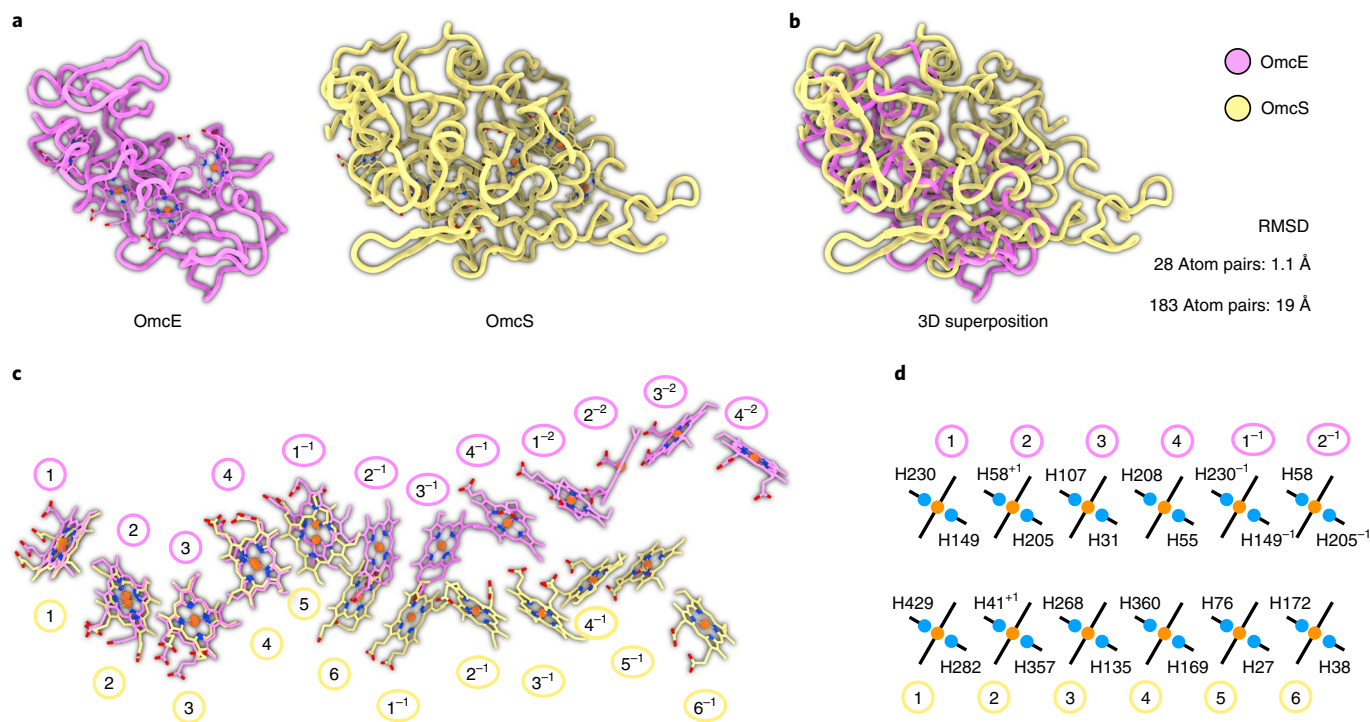


Fig. 2 | OmcE versus OmcS, very different protein structures but almost identical haem packing. **a**, Backbone traces of single OmcE and OmcS subunits. Haem molecules are shown as sticks. **b**, Alignment of OmcE and OmcS proteins. The RMSDs of aligned and total atom pairs are shown. **c**, Comparison of haem chains in OmcE and OmcS filaments. The OmcS filament is aligned to the OmcE subunit on the left containing haems 1–4. **d**, Bis-histidine coordinations for the six haems aligned in **c**. Iron atoms in haem are shown as orange circles, and imidazole side chains of the histidines are represented by blue circles.

the RMSD increased to 19 Å between 185 atom pairs (Fig. 2a,b). The four CxxCH haem-binding motifs and the additional distal histidines coordinating the haems accounted for almost all of the residues in the 28 C_α pairs that could be aligned with a 1.1 Å RMSD

between OmcE and OmcS. To the best of our knowledge, the coordination of a haem in one subunit by a histidine in an adjacent subunit in both the OmcE and OmcS filaments seems to be unique among all *c*-type cytochrome structures solved to date. The conservation

of haem arrangements between OmcS and OmcE raises the possibility that the haems are dictating the protein fold rather than the protein determining the position of the haems. This would be consistent with the exquisite conservation of haem arrangements, despite a lack of any sequence or structural homology between OmcS and OmcE.

There was one exception to the conserved 3D histidine alignment: OmcE-H58 was structurally aligned in three dimensions to OmcS-H41 at haem 2, where they each coordinated haems of the adjacent protein subunit (Fig. 2d). However, in a sequence-based alignment (Extended Data Fig. 6a), OmcE-H58 aligned to OmcS-H172. This was due to the backbone positions of OmcE-H58 and OmcS-H172 being close, but their side-chain conformations diverged to coordinate the next monomer's haem 2⁺¹ in OmcE and haem 6 in OmcS, respectively (Fig. 2d).

Stacking arrangement of haem pairs. Given how well the four haems could be superimposed between OmcE and OmcS, we asked whether this represented a preferred haem–haem pairing motif used in proteins capable of efficient electron transfer. For example, closely related redox partners, such as cytochrome c554 and hydroxylamine oxidoreductase (HAO), have conserved tetrahaem cores with structural similarities⁵⁶. Similarly, chains of haem have a similar arrangement in multihaem proteins involved in conversion of nitrogen and sulfur compounds, despite substantial divergence in overall protein structures and sequences⁵⁷.

To compare OmcE haem orientations with haem *c* pairs available in the Protein Data Bank (PDB), we looked at all 853 entries containing haem *c* (HEC) as a ligand, and retained all pairs with a minimum edge-to-edge distance ≤ 6 Å. We applied a 6 Å distance limit as an arbitrary cut-off, because longer distances are less efficient in regard to electron transfer processes. We defined the rotation angle in a haem pair as the rotation required, along with a translation, to bring one haem into alignment with that of the other haem in the pair, including haem side chains (Fig. 3a). In OmcS and OmcE filaments, all haem pairs were either 'parallel-stacked'—that is, at an angle of nearly 180°—or rotated from each other by about 140°. When we looked at the rotation angle for the haems in our PDB dataset and plotted these against the edge-to-edge distances between each HEC pair, a clear clustering pattern was observed (Fig. 3b). This suggested that there are preferred haem–haem orientations in most known multihaem structures. Most of the minimum distances fell within the range 3–4 Å, suggesting strong selection for a few key orientations at haem–haem distances supporting efficient electron transfer.

Similar to OmcE and OmcS, rotation angles of porphyrin orientations in HEC pairs identified from the PDB data mostly clustered near 170–180° and 110–140°, with a smaller clustering around 50–60° for more distantly spaced haems. Interestingly, with only one exception, there were no haem–haem pairs with an angle of rotation 0–5.5°. The exception, PDB 6BTM, was done at a resolution of 3.4 Å where the haem cannot be positioned unambiguously if previous knowledge from high-resolution crystal structures has not been used.

The clustering we identified suggests that what was previously referred to in the literature as 'parallel' haem pairs would be more accurately described as 'anti-parallel' pairs: one haem must be rotated nearly 180° to align with the neighbouring haem. Similarly, a much larger number of haem pairs was identified with rotation angle 110–140° compared with those in the minor cluster at a roughly complementary angle of 50–60°. The minimum edge-to-edge distances were also greater in the 50–60° cluster, suggesting an orientation preference for densely packed bis-coordinated haem pairs at obtuse angles. Notably, all haem pairs of OmcS and OmcE that form cytochrome filaments fell into the two major clusters characteristic of closely spaced haems.

Post-translational modifications in OmcE. In OmcS filaments, two modification sites (T82 and T119) were directly detected in the cryo-EM map (EMD-9046), even though additional densities associated with modifications were not obvious when looking at the surface of the map. Unlike OmcS, OmcE filaments have readily apparent multiple additional densities on the filament surface due to post-translational modifications, which we hypothesize are glycosylations (Extended Data Fig. 6b,c). Although we cannot unambiguously determine the identity of the post-translational modifications, due to the flexibility and limited resolution of these putative glycans, potential modification sites included S83, N86, N87, N132 and T184. The presence of multiple post-translational modifications would explain discrepancies between the predicted mass of OmcE and its behaviour as a larger-than-expected protein in both SDS–polyacrylamide gel electrophoresis (SDS–PAGE) and MALDI coupled with time-of-flight mass spectrometry (MALDI–TOF)¹⁸. Because sugars do not bind SDS, the decreased mass/charge ratio of glycosylated OmcE would slow migration and the addition of between five and ten sugar molecules would account for the extra ~1–2 kDa reported in MALDI¹⁸. Glycosylation would also be consistent with the presence of a 17-gene cluster immediately downstream of *omcE* that contains glycosyltransferases, nucleotide-sugar epimerases and transporters commonly associated with translocation of sugars to the periplasm (Extended Data Fig. 7).

Extracellular pili and DNA in sheared preparations. Cell appendages, such as bacterial pili^{58,59}, typically remain in the supernatant after sample centrifugation at 8,000g for 30 min in preparation for deposition on cryo-EM grids, but many filaments segregated to the pellet during centrifugation. For a more complete characterization of filaments produced in our experiments, we used a milder centrifugation (5,000g for 1 min) to remove cell debris and visualized all extracellular filaments without using DNase I treatment. In 5,665 cryo-EM images from these preparations, four distinct filament species were observed. We classified these filaments using two-dimensional (2D) averages (Fig. 4a,b): (1) OmcE filaments ~40 Å in diameter; (2) mutated OmcS or OmcS-like filaments ~50 Å in diameter; (3) Type IV pili ~75 Å in diameter; and (4) B-DNA filaments ~25 Å in diameter.

Type IV pili were not previously observed in preparations used to determine the atomic structure of wild-type OmcS filaments²⁶, possibly due to centrifugation steps used in that study. Type IV pili from *G. sulfurreducens*, composed of PilA-N and PilA-C chains, were previously detected only when PilA was overexpressed²⁸. In our experiments, we did not overexpress PilA-N/C but still observed these filaments. If pili are involved in OmcS maturation or secretion, it is possible that mutations in OmcS would affect periplasmic incorporation of haem or retraction of PilA.

We generated a 3D reconstruction of native PilA filaments with a resolution of ~4.1 Å, yielding an unambiguous tracing of both PilA-N and PilA-C chains in the cryo-EM map (Fig. 4c and Supplementary Table 1) consistent with the previously reported structure of the overexpressed pilus²⁸. The presence of PilA-N/C type IV pili is also consistent with their high sequence coverage from mass spectrometry of filament isolates (Extended Data Fig. 5).

Conductive bacterial appendages were previously proposed to be type IV pili comprised solely of the PilA-N chain⁶⁰, despite the lack of a power spectrum, 2D averages or 3D reconstructions verifying their identity in cryo-EM or negative-stain images. We analysed previously published images of putative PilA-N filaments from Malvankar et al.⁶¹ and showed that they are OmcS filaments, based upon the power spectrum observed (Extended Data Fig. 8). Models for electron conduction in putative PilA-N filaments are predicated on the assumption of close-stacking aromatic rings^{24,60,62–65}. However, these models mainly rely on a 2006 study of the type IV pilus from *Neisseria gonorrhoeae*, which fitted a crystal structure

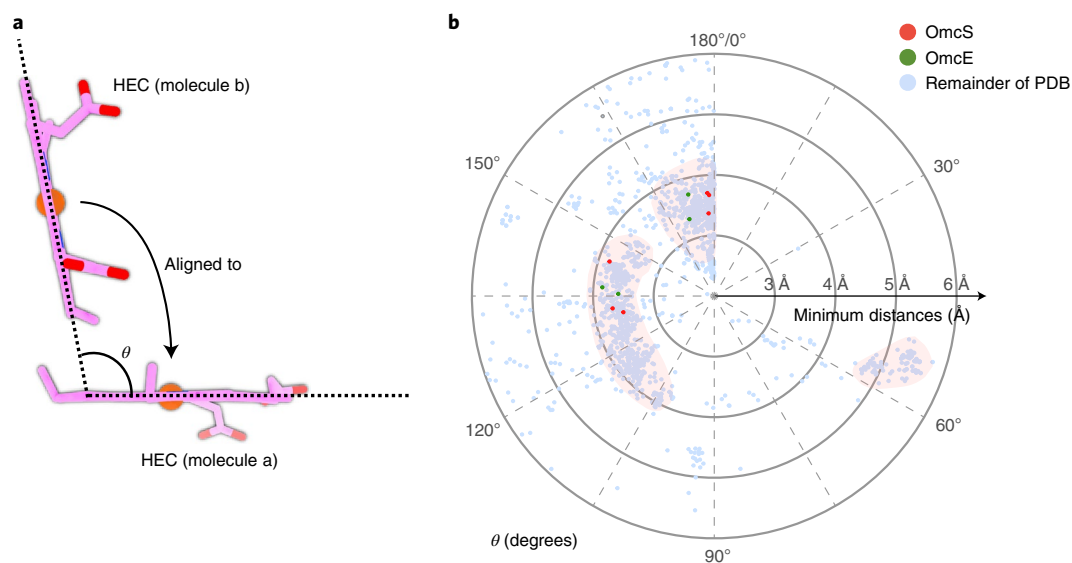


Fig. 3 | Orientation plot for HEC pairs. **a**, One haem in a pair can be aligned to the other by a rotation and a translation. The rotation angle, θ is shown. For example, as shown in Fig. 2c, rotation angle θ between haem 1 and haem 2 is -130° , between haem 2 and haem 3 is -175° and between haem 3 and haem 4 is -140° . **b**, The haem (HEC only, ligand ID: HEC) pairs in all PDB structures were analysed. Minimum distances refer to the least distance between haem pairs, regardless of atom type. The angle, θ was determined from the alignment rotation matrix between haem pairs. For example, $\theta=0^\circ$ means that two haems are perfectly parallel while $\theta=180^\circ$ means that two haems are perfectly anti-parallel (flipped) during alignment. All haem pairs with minimum distance $\leq 6 \text{ \AA}$ are shown. Haem pairs in OmcE and OmcS filaments are highlighted in green and red, respectively.

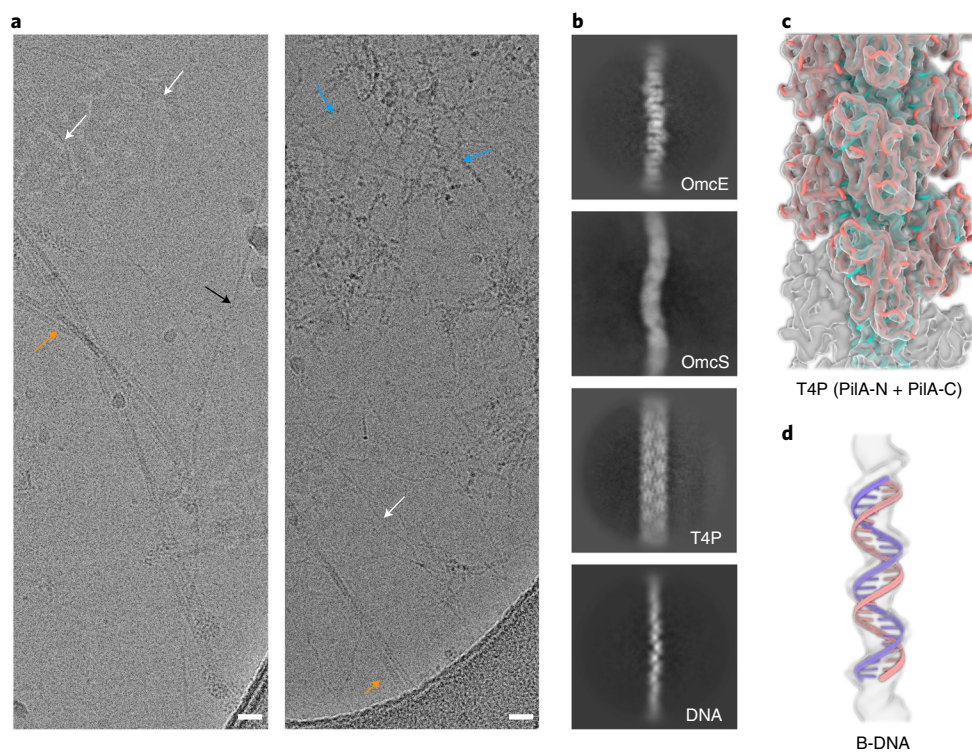


Fig. 4 | Mixtures of OmcS variant (H357M), extracellular T4P, DNA and OmcE filaments. **a**, Representative cryo-EM image of filaments sheared and precipitated from an overproducing OmcS-H357M variant strain of *G. sulfurreducens*, taken from the 17,105 images recorded. The sample was not treated with DNase I before freezing and was not centrifuged to remove aggregates as in Fig. 1. Other than OmcS filaments, other species of filaments were observed and labelled correspondingly: OmcE filaments (black arrow), OmcS filaments (blue arrows), PiliA-N-C type IV pili (orange arrows) and extracellular B-form DNA (white arrows). Scale bar, 200 \AA . **b**, 2D averages of the four different filaments in **a**, showing that these various filaments are readily distinguishable. **c**, A $\sim 4.1 \text{ \AA}$ cryo-EM reconstruction of type IV pili, with ribbon model of the PiliA subunits containing two chains, PiliA-N (cyan) and PiliA-C (orange). **d**, A $\sim 10 \text{ \AA}$ cryo-EM reconstruction of DNA filaments showing a clear pitch of $\sim 36 \text{ \AA}$ with ribbon model of B-DNA.

into a very-low-resolution (12.5 Å) cryo-EM reconstruction⁶⁶. High-resolution structures of bacterial type IV pili^{58,59,67–69} have subsequently become available revealing that there is a partial melting of the N-terminal helix, a feature that would prevent continuous stacking of aromatic residues in the *Geobacter* model. Furthermore, high-resolution structures of the *Geobacter* type IV pilus, obtained using either overexpression of PilA-N and PilA-C²⁸ or native expression as we report here, also show partial melting of the N-terminal helix. Based on these higher-resolution structures, we conclude that there is no evidence that *Geobacter* PilA behaves differently from any other bacterial type IV pilins studied to date.

One recent study proposed that unidentified ~3 nm filaments observed in *G. sulfurreducens* cryo-EM preparations used to determine the larger ~4–5 nm OmcS structure were ‘presumably’ composed of PilA-N²⁵, in seeming contradiction to the 7.5 nm PilA-N/C filament identified here and in other studies²⁸. Several points call into question that proposed identification. First, electron micrographs from that study²⁵ were not made public, which precludes comparisons with OmcE or DNA structures. Second, we contend that because the PilA-N chain is highly hydrophobic⁷⁰ (Extended Data Fig. 9), a filament formed from PilA-N alone would most probably be insoluble²⁸. We have never observed, by cryo-EM, a filament composed solely of the PilA-N chain.

When DNase I was not added to our preparations, a large number of DNA filaments was seen in all micrographs (Fig. 4a,b). 2D averages clearly show the ~36 Å pitch (Fig. 4b) expected from B-form DNA, and a ~10-Å-resolution 3D reconstruction was fit well with a B-DNA atomic model (Fig. 4d). Such DNA may be due to cell lysis during shearing, or having been secreted as a component of the extracellular matrix during biofilm formation⁷¹. It has not escaped our notice that this ubiquitous DNA is similar in dimensions and morphology to many of the filaments previously described as pili nanowires, and propose that DNA might contribute to limited conductivity in biofilms, the extracellular matrix or individual filaments⁷². Future studies isolating conductive filaments should include DNase as a control measure, to discount the contribution of extracellular DNA to the observed properties.

Discussion

We determined the atomic structure of a previously uncharacterized cytochrome filament composed of OmcE and show that, in addition to OmcS polymers, other extracellular filaments are produced by *G. sulfurreducens*.

Although the overall protein fold, size and helical pitch of hexahaem OmcS and tetrahaem OmcE are quite different, there is a high degree of alignment of the four haems of OmcE with the first four in OmcS, as well as the corresponding CxxCH motifs that incorporate these haems into the cytochrome. Both proteins lack substantial amounts of secondary structure, a feature consistent with many multi-haem *c*-type cytochromes. However, lacking secondary structure does not mean disordered, because disordered regions of the protein would not appear in the averaged 3D cryo-EM map and the full chains of OmcS and OmcE can be traced from these maps. Mutations, insertions and deletions in loops and coils could thus easily occur, providing they did not perturb the local coordination of haem groups. This decreased selective pressure on most residues could explain the high mutation rate observed within multihaem cytochrome sequences, such as between cytochromes of closely related *G. sulfurreducens* PCA and KN400 strains where 25.8 non-synonymous changes per 1,000 bases were found in OmcE compared with an average of only 5.6 per 1,000 across the rest of the proteome⁷³.

A lack of secondary structure content is a feature seen in other electron-transporting, multihaem cytochromes such as *Shewanella baltica* MtrA, in which 80% of the protein is loops⁷⁴, similar to other MtrA homologues⁷⁵. MtrA, a decahaem cytochrome, also shares

the paired-stack haem arrangement motif with OmcS and OmcE filaments, with haem pairs falling into the two major motif clusters (Fig. 3b), and it functions as a transmembrane electron conduit in *Shewanella* spp. This motif is present in other multihaem cytochromes, such as *S. oneidensis* small tetrahaem cytochrome (STC/CctA) and *E. coli* NrfB, both of which lack substantial sequence identity with MtrA⁷⁴. The low sequence similarity and high fidelity of the haem arrangement between these proteins suggest that haem packing is the functional feature conferring high conductivity and rapid respiration rates. Indeed, electron transfer rates in the direction of extracellular electron transfer are calculated to be similar in OmcS filaments and the MtrAB transmembrane complex⁷⁶. Moreover, the clustering of haem pair rotation angles and edge-to-edge distances (Fig. 3b) reveals conserved arrangements of haem across all domains of life. This arrangement could be preferred for biosynthetic reasons—for example, representing an optimal solution to a steric or reaction selectivity limitation on the density of haem incorporation into the apoprotein. The anti-parallel orientation of haem pairs in the 110–140° and 170–180° clusters suggests such a preference for opposing thioether linkages within haem pairs. Alternatively, the arrangement could be optimal for long-range electron transport and represent a selective pressure for evolution. Whether this class of multihaem cytochromes resulted from convergent or divergent evolutionary processes is unclear, but the haem structure appears highly conserved in proteins requiring rapid electron transport for their function.

What is the role of the modifications observed on the exterior of the OmcE and OmcS filaments? Glycans on the surface might protect against protease cleavage, minimize damage from free radicals produced as a by-product of cytochrome peroxidase activity or alter binding to metal oxide electron acceptors. In archaeal filaments, it has been suggested that glycosylation plays a major role in protection of these extracellular appendages in extreme environments⁷⁷. Regardless of their function, the potential of bis-coordinated haems should be relatively insensitive to the protein environment surrounding the haem, let alone to distant modifications such as glycosylation. We do speculate, however, that the material coating OmcE could cause artefacts during laboratory conductivity measurements, by increasing contact resistance due to greater charge tunnelling distances.

Previously, overexpression of PilA-N and PilA-C was used to produce extracellular PilA filaments²⁸. We confirm here that the native PilA pilus of *G. sulfurreducens* is composed of two chains, PilA-N and PilA-C, in strains in which the only genetic changes are residues within OmcS. This PilA structure was previously proposed to form a periplasmic pseudo-pilus, possibly to aid export of cytochrome filaments^{26,28}. Whatever their true function in *G. sulfurreducens*, PilA pili and cytochrome filament levels are evidently tightly linked. Mutations affecting OmcS assembly allowed easier detection of PilA pili and OmcE polymers, while *pilA-N* mutations in previous studies decreased production of OmcS polymers. Given the importance of PilA in controlling *omcS*, *omcB*, *omcAHG*, *omcOP* and *pgcA* expression via PilS/PilR-dependent and cyclic di-GMP/cyclic AMP-GMP-dependent regulatory networks^{49,50,78}, changes in type IV pilin subunits should always be expected to affect electron transfer phenotypes and production of conductive appendages in *Geobacter* experiments.

The *in situ* identification of extracellular filaments from *G. sulfurreducens* has largely been based on atomic force microscopy (AFM) height/diameter measurements, although the size of presumptive PilA-N pili has varied among fixed (~3 nm)⁸, desiccated (3–5 nm)²⁰, air-dried (~3 nm)⁷⁹, spin-coated (~4–6 nm)⁸⁰, solvent-evaporated (~2 nm)⁷⁰ and humidified (3–4 nm)²⁴ preparations on highly oriented pyrolytic graphite, Pt, Au and mica. We do not think that these measurements are well suited for identification. Negative-stain transmission electron microscopy (TEM)⁸¹

and AFM⁸² of dried samples usually does not preserve structure, because shrinkage can readily occur. Quantitative analysis in TEM has shown that the thickness can be reduced to 60% of the native value⁸³. Strong adsorption to substrates combined with dehydration can severely flatten filaments, affecting height measurements in AFM. Tip-convolution artefacts are common in AFM even when measurements are done in solution⁸⁴, which impacts observed filament diameter, and AFM of dried specimens usually does not reveal the internal structure or periodicities. Even during high-resolution cryo-EM of frozen/hydrated proteins, interpretation of diameter is not simple given the contrast-transfer function and ambiguities in defining outer edges from noisy images. Accurate dimensions can instead be derived from atomic models built into high-resolution cryo-EM maps for comparison (Extended Data Fig. 10), or descriptions can be based upon more robust measures of periodicities within these filaments such as helical pitch or rise per subunit.

Having an atomic structure, the definition of diameter can still be ambiguous. The atomic structure for OmcS filaments has a diameter of 5.0–7.5 nm (Extended Data Fig. 10)^{25,26}. In the atomic structure, while the ‘local’ diameter of OmcS is 5.0 nm, the smallest cylinder that would include all sinusoidal undulations would have a diameter of ~7.5 nm (Extended Data Fig. 10). Even a value of 5.0 nm is an approximation, because OmcS does not have a smooth surface and contains hydrogen atoms that enlarge the diameter, and that does not consider the larger hydrodynamic radius including tightly bound waters. As an example, despite these atomic predictions of a 5–7 nm diameter, a recent paper²⁷ measured dried OmcS filaments by AFM at 3.5 nm. Due to the growing diversity of extracellular filaments, each of potential diameter 2–7 nm (including DNA, pili, OmcE, OmcZ and OmcS), additional information will now be required for conclusive identification in experiments. The understanding of long-range electron transport in bacteria will probably advance when conductivity data can be reliably linked to the internal structure of the filament under analysis. At the present time, however, the likelihood that published *G. sulfurreducens* strains produce multiple extracellular filaments, and the presence of DNA in most samples, means that measures of conductivity attributed to a specific protein need to be treated with some caution.

There are more than 75 other multihaem cytochromes in the *G. sulfurreducens* genome alone, many with an operon structure similar to OmcS, OmcE or OmcZ. Since we now know that the helical symmetry for multihaem cytochrome filaments appears to be determined by the haem arrangement rather than by details of the protein fold, a possibility exists that the bundles presumed to be OmcS might actually be composed of the hexahaem cytochrome GSU2501, which was also detected in the sample by mass spectrometry (Extended Data Fig. 5). This will be a question for future studies. Finding homologues or predicting whether related organisms are capable of producing similar extracellular filaments is severely limited by the rapid rate of multihaem protein sequence divergence. Our work suggests that unexpected commonalities exist among these cytochromes, including conserved haem arrangements and haem-binding motifs. The early success with machine learning-based tools such as AlphaFold means that it might soon be possible to scan genomes of distant relatives or uncultivated genera for structural homologues based on the universal characteristics of this growing cytochrome nanowire family.

Methods

***G. sulfurreducens* mutant construction and filament preparation.** *Geobacter sulfurreducens* PCA was obtained from the DSMZ culture collection (no. DSMZ 12127). *G. sulfurreducens* colonies were isolated from agar plates (1.5%) in anoxic basal medium, with acetate (20 mM) as the electron donor and fumarate (40 mM) as the electron acceptor, under a H₂/CO₂/N₂ (5:20:75) atmosphere in an anaerobic workstation 500 (Don Whitley). The pH of the medium was adjusted to 6.8, buffered with 2 g l⁻¹ NaHCO₃ and purged with N₂/CO₂ gas (80:20) passed over a

heated copper column to remove trace oxygen. Liquid cultures were grown without the addition of agar. All cultures were grown at 30 °C.

The *omcS* gene was deleted using a SacB-sucrose counterselection strategy to generate a scarless gene deletion⁸⁵. The primers used to amplify and clone the flanking regions of *omcS* to generate the *omcS* deletion mutant are listed in Supplementary Table 2. The ~1.5 kb flanking sequences of *omcS* were combined by overlap PCR and blunt-end cloned into SacB-encoding plasmid pK18mobsacB using SmaI.

The *omcS* sequences with mutations encoding variants H38M, H41M and H357M were synthesized and cloned into the pTwist-Amp vector by Twist Biosciences (listed in Supplementary Table 3). Expression of *omcS* mutants was under the control of a moderate- (*acpP*, pTn7m) or higher-expression (*ppcA* pTn7-Geo7) promoter when subcloned into either pTn7m or pTn7-Geo7 using NdeI and ApaLI. The *omcS* mutant genes were integrated with 25 base pairs downstream of the *glmS* gene in the *omcS* deletion strain, using a targeted Tn7-based strategy by tri-parental mating with *E. coli* conjugative donor strain MFDpir and Tn7 mobilization machinery encoded in pTns3 (refs. ^{54,86}).

For all experiments, *G. sulfurreducens* variants were revived from frozen stocks anaerobically and grown from single-colony picks on 1.5% agar plates (NBFA medium) containing 20 mM acetate donor and 40 mM fumarate acceptor⁸⁷. NBFA liquid medium is composed of 20 mM acetate donor and 40 mM fumarate acceptor, 0.38 g l⁻¹ potassium chloride, 0.2 g l⁻¹ ammonium chloride, 0.069 g l⁻¹ monosodium phosphate, 0.04 g l⁻¹ calcium chloride dihydrate, 0.2 g l⁻¹ magnesium sulfate heptahydrate, 2.0 g l⁻¹ sodium bicarbonate and 10 ml of mineral mix⁸⁸. Resazurin and cysteine were omitted. NBFA media were sterilized and degassed using 80:20 N₂/CO₂. All chemicals were purchased from Fisher Scientific unless otherwise noted.

Cells from fully grown cultures of *G. sulfurreducens* were pelleted after reaching stationary phase via centrifugation at 4,600g for 25 min at 4 °C. Cells were resuspended in 50 mM Tris-HCl (pH 7.5) followed by mechanical shearing to detach the extracellular filaments using a Waring Commercial Blender (no. 7011 S) at a low-speed setting for 5 min⁸⁶. Centrifugation at 10,000g for 15 min removed cells, and filaments were precipitated from the supernatant with 10% ammonium sulfate overnight at 4 °C while stirring, followed by centrifugation at 17,000g for 1 h. The final filament pellets were resuspended in 10 ml of Tris-HCl buffer. To help remove contaminants, filament samples were dialysed with 300 kDa dialysis tubing (Biotec CE, Repligen) against ultra-pure water (pH 4.3).

Gel analysis of filament samples. To separate them via sodium-dodecyl sulfate unambiguously (SDS-PAGE), filament samples were mixed with reducing sample buffer with 0.3% w/v final concentration of SDS and 1.5% v/v final concentration of β-mercaptoethanol (TCI America). All samples were heated for 5 min at 100 °C and then cooled and spun at 2,500g for 1 min before loading into the gel. Filament samples were run on 4–16% Tricine-SDS-PAGE gels⁸⁹ prepared using Acryl/Bis (37.5:1.0, 40% w/v) solution (VWR), with an initial voltage of 30 V for 20 min and subsequent voltage step of 200 V for 3 h. A Spectra multicolour broad-range protein ladder (ThermoFisher) was used to reference the molecular weight of protein bands. Gels were stained with either silver stain⁹⁰ or 3,3',5,5'-tetramethylbenzidine (TMB)⁹¹ after washing with ultra-pure water. β-Mercaptoethanol addition was omitted for haem (TMB) staining samples.

In-solution tryptic digestion. The filament samples were centrifuged at 8,000g for 30 min, and supernatants were dialysed with 300 kDa dialysis tubing against ultra-pure water. Concentrator 30 kDa units (Spin-X UF, Corning) were used to obtain a protein concentration of >0.2 mg ml⁻¹ and remove remnant salts and other small-molecular-weight contaminants. Filaments obtained following concentration were digested in solution using Trypsin Gold (Promega). Following the Promega protocol, 100 µg of trypsin was resuspended in 50 mM acetic acid to reach 1 µg µl⁻¹ and diluted to 20 µg ml⁻¹ in a solution of 40 mM ammonium bicarbonate in 10% acetonitrile. Fifty microlitres of filament samples was reduced by 5 µl of 100 mM DL-dithiothreitol (Sigma-Aldrich), and samples were heated for 5 min at 95 °C followed by 20 min incubation at 37 °C. Next, 20 µl of 100 mM iodoacetamide (Sigma-Aldrich) was added to all filament samples with incubation in the dark for 1 h. The reaction was then diluted with 150 µl of 50 mM Tris-HCl (pH 7.5) buffer before the addition of 10 µl of trypsin and overnight incubation at 37 °C.

Mass spectrometry of filament samples. The in-solution tryptic digestion of filament samples was quenched after overnight incubation by the addition of 25 µl of 5% formic acid, before characterization by matrix-assisted laser desorption/ionization (MALDI) time-of-flight (TOF)/TOF (UltrafleXtreme, Bruker) in positive-ion mode. The matrix solution was freshly prepared with a saturated solution of α-cyano-4-hydroxycinnamic acid (Sigma-Aldrich) dissolved in a 2:1 solution of ultra-pure water/acetonitrile⁹². The collected mass spectra were analysed using mMass protein identification software^{92–94}.

Cryo-EM conditions and image processing. The cell appendage sample (~2.0–2.5 µl) was applied to glow-discharged lacey carbon grids and then plunge-frozen using an EM GP Plunge Freezer (Leica). Cryo-EMs were collected on a 300 keV Titan Krios with a K3 camera (University of Virginia) at 1.08 Å per pixel and a total dose of ~50 e Å⁻². Motion corrections and contrast transfer function (CTF)

estimations were done in cryoSPARC^{95–97}. Particles were auto-picked by ‘Filament Tracer’. All auto-picked particles were subsequently 2D classified with multiple rounds, and all particles in bad 2D averages were removed. The OmcE dataset had 346,826 particles remaining with a shift of 35 pixels between adjacent boxes, while the PilA dataset had 112,011 particles remaining with a shift of six pixels. Potential helical symmetries were calculated from an averaged power spectrum for each filament species generated from the raw particles. For each filament species, the actual helical symmetry was then determined in cryoSPARC by trial and error until amino acid side chains and the hand of α -helices were seen^{98,99}. The resolution of each reconstruction was estimated by Map:Map FSC, Model:Map FSC and d_{90} (ref. ¹⁰⁰). Final volumes were then sharpened with a negative B-factor automatically estimated in cryoSPARC, and the statistics are listed in Supplementary Table 3.

Model building of PilA filaments. The density corresponding to a single PilA complex was segmented from the experimental cryo-EM density using Chimera¹⁰¹. A single PilA (PilA-N + PilA-C) from 6VK9 was used as the starting model, and real space refined in PHENIX¹⁰². Using the determined helical symmetry, a filament model was generated in Chimera and refined against the full cryo-EM map using PHENIX real-space refinement. MolProbity¹⁰³ was used to evaluate the quality of the filament model. The refinement statistics are shown in Supplementary Table 1. The RMSD between our filament model and 6VK9 was 0.3 Å over 163 atom pairs.

Model building of OmcE filaments. The hand of OmcE filaments was determined by the hand of an α -helix. The hand assignment also agreed with the AlphaFold2 (ref. ⁵³) models of OmcE and its three structurally related homologues. To determine which cytochrome protein best fit into the cryo-EM map, the fit of OmcE and homologues were separately estimated and real space refined against the map in PHENIX¹⁰². OmcE was the best fit with a large RSCC difference compared with the second-best fit protein, OmcP (0.7 versus 0.35). To better refine haem-interacting areas at this resolution, bond/angle restraints for the haem molecule itself (His-Fe) and Cys-haem thioester bonds were restricted based on the geometries obtained in high-resolution crystal structures such as NrfB¹⁰⁴ (PDB 2P0B) and NrfHA¹⁰⁵ (PDB 2J7A). MolProbity¹⁰³ was used to evaluate the quality of the filament model. The refinement statistics are shown in Supplementary Table 1.

Structural analysis of HEC pairs. All structural coordinates with HEC were downloaded from PDB. All potential haem pairs were then filtered with a minimum distance ≤ 6 Å, with the ‘contact’ command in UCSF-ChimeraX¹⁰⁶. For each qualified pair, the rotation matrix between two haems was generated in ChimeraX using the ‘align’ command. Rotation angle θ was then calculated from the rotation matrix with the following equation, where tr is the trace of the rotation matrix:

$$|\theta| = \arccos\left(\frac{\text{tr}(R) - 1}{2}\right)$$

Reporting summary. Further information on research design is available in the Nature Research Reporting Summary linked to this article.

Data availability

The 3D reconstruction for OmcE has been deposited in the Electron Microscopy Data Bank with accession code EMD-25879, and the atomic model has been deposited in PDB with accession code 7TFS. The 3D reconstruction for PilA-N/C has been deposited in the Electron Microscopy Data Bank with accession code EMD-25881, and the atomic model has been deposited in PDB with accession code 7TGG. Other atomic models used in the study were PDB 2P0B, 2J7A and 6VK9.

Received: 23 January 2022; Accepted: 23 May 2022;
Published online: 7 July 2022

References

- Lovley, D. R., Phillips, E. J. P., Gorby, Y. A. & Landa, E. R. Microbial reduction of uranium. *Nature* **350**, 413–416 (1991).
- Lloyd, J. R., Sole, V. A., Van Praagh, C. V. & Lovley, D. R. Direct and Fe(II)-mediated reduction of technetium by Fe(III)-reducing bacteria. *Appl. Environ. Microbiol.* **66**, 3743–3749 (2000).
- Ortiz-Bernad, I., Anderson, R. T., Vrionis, H. A. & Lovley, D. R. Vanadium respiration by *Geobacter metallireducens*: novel strategy for in situ removal of vanadium from groundwater. *Appl. Environ. Microbiol.* **70**, 3091–3095 (2004).
- Lovley, D. R., Coates, J. D., BluntHarris, E. L., Phillips, E. J. P. & Woodward, J. C. Humic substances as electron acceptors for microbial respiration. *Nature* **382**, 445–448 (1996).
- Bond, D. R., Holmes, D. E., Tender, L. M. & Lovley, D. R. Electrode-reducing microorganisms that harvest energy from marine sediments. *Science* **295**, 483–485 (2002).
- Summers, Z. M. et al. Direct exchange of electrons within aggregates of an evolved syntrophic coculture of anaerobic bacteria. *Science* **330**, 1413–1415 (2010).
- Morita, M. et al. Potential for direct interspecies electron transfer in methanogenic wastewater digester aggregates. *mBio* **2**, e00159–11 (2011).
- Reguera, G. et al. Extracellular electron transfer via microbial nanowires. *Nature* **435**, 1098–1101 (2005).
- Lovley, D. R., Holmes, D. E. & Nevin, K. P. Dissimilatory Fe(III) and Mn(IV) reduction. *Adv. Microb. Physiol.* **49**, 219–286 (2004).
- Lovley, D. R. Bioremediation – anaerobes to the rescue. *Science* **293**, 1444–1446 (2001).
- Wall, J. D. & Krumholz, L. R. Uranium reduction. *Annu. Rev. Microbiol.* **60**, 149–166 (2006).
- Cardenas, E. et al. Microbial communities in contaminated sediments, associated with bioremediation of uranium to submicromolar levels. *Appl. Environ. Microbiol.* **74**, 3718–3729 (2008).
- Shrestha, P. M. et al. Syntrophic growth with direct interspecies electron transfer as the primary mechanism for energy exchange. *Environ. Microbiol. Rep.* **5**, 904–910 (2013).
- Cao, X. et al. A new method for water desalination using microbial desalination cells. *Environ. Sci. Technol.* **43**, 7148–7152 (2009).
- Gong, Y. et al. Benthic microbial fuel cell as direct power source for an acoustic modem and seawater oxygen/temperature sensor system. *Environ. Sci. Technol.* **45**, 5047–5053 (2011).
- Lovley, D. R. et al. *Geobacter*: the microbe electric’s physiology, ecology, and practical applications. *Adv. Microb. Physiol.* **59**, 1–100 (2011).
- Rabaey, K., Girguis, P. & Nielsen, L. K. Metabolic and practical considerations on microbial electrosynthesis. *Curr. Opin. Biotechnol.* **22**, 371–377 (2011).
- Mehta, T., Coppi, M. V., Childers, S. E. & Lovley, D. R. Outer membrane c-type cytochromes required for Fe(III) and Mn(IV) oxide reduction in *Geobacter sulfurreducens*. *Appl. Environ. Microbiol.* **71**, 8634–8641 (2005).
- Nevin, K. P. et al. Anode biofilm transcriptomics reveals outer surface components essential for high density current production in *Geobacter sulfurreducens* fuel cells. *PLoS ONE* **4**, e5628 (2009).
- Malvankar, N. S. et al. Tunable metallic-like conductivity in microbial nanowire networks. *Nat. Nanotechnol.* **6**, 573–579 (2011).
- Malvankar, N. S. & Lovley, D. R. Microbial nanowires for bioenergy applications. *Curr. Opin. Biotechnol.* **27C**, 88–95 (2014).
- Wang, O., Zheng, S., Wang, B., Wang, W. & Liu, F. Necessity of electrically conductive pili for methanogenesis with magnetite stimulation. *PeerJ* **6**, e4541 (2018).
- Clark, M. M. & Reguera, G. Biology and biotechnology of microbial pilus nanowires. *J. Ind. Microbiol. Biotechnol.* **47**, 897–907 (2020).
- Liu, X., Walker, D. J. F., Nonnenmann, S. S., Sun, D. & Lovley, D. R. Direct observation of electrically conductive pili emanating from *Geobacter sulfurreducens*. *mBio* <https://doi.org/10.1128/mBio.02209-21> (2021).
- Filman, D. J. et al. Cryo-EM reveals the structural basis of long-range electron transport in a cytochrome-based bacterial nanowire. *Commun. Biol.* **2**, 219 (2019).
- Wang, F. et al. Structure of microbial nanowires reveals stacked hemes that transport electrons over micrometers. *Cell* **177**, 361–369 (2019).
- Yalcin, S. E. et al. Electric field stimulates production of highly conductive microbial OmcZ nanowires. *Nat. Chem. Biol.* **16**, 1136–1138 (2020).
- Gu, Y. et al. Structure of *Geobacter* pili reveals secretory rather than nanowire behaviour. *Nature* **597**, 430–434 (2021).
- Lebedev, N., Stroud, R. M., Yates, M. D. & Tender, L. M. Spatially resolved chemical analysis of *Geobacter sulfurreducens* cell surface. *ACS Nano* **13**, 4834–4842 (2019).
- Yalcin, S. E. & Malvankar, N. S. The blind men and the filament: understanding structures and functions of microbial nanowires. *Curr. Opin. Chem. Biol.* **59**, 193–201 (2020).
- Holmes, D. E. et al. Microarray and genetic analysis of electron transfer to electrodes in *Geobacter sulfurreducens*. *Environ. Microbiol.* **8**, 1805–1815 (2006).
- Richter, H. et al. Cyclic voltammetry of biofilms of wild type and mutant *Geobacter sulfurreducens* on fuel cell anodes indicates possible roles of OmcB, OmcZ, type IV pili, and protons in extracellular electron transfer. *Energy Environ. Sci.* **2**, 506–516 (2009).
- Shelobolina, E. S. et al. Importance of c-Type cytochromes for U(VI) reduction by *Geobacter sulfurreducens*. *BMC Microbiol.* **7**, 16 (2007).
- Voordeckers, J. W., Kim, B.-C., Izallalen, M. & Lovley, D. R. Role of *Geobacter sulfurreducens* outer surface c-type cytochromes in reduction of soil humic acid and anthraquinone-2,6-disulfonate. *Appl. Environ. Microbiol.* **76**, 2371–2375 (2010).
- Smith, J. A., Lovley, D. R. & Tremblay, P. L. Outer cell surface components essential for Fe(III) oxide reduction by *Geobacter metallireducens*. *Appl. Environ. Microbiol.* **79**, 901–907 (2013).

36. Huang, L., Liu, X., Ye, Y., Chen, M. & Zhou, S. Evidence for the coexistence of direct and riboflavin-mediated interspecies electron transfer in *Geobacter* co-culture. *Environ. Microbiol.* **22**, 243–254 (2020).
37. Liu, X., Zhuo, S., Rensing, C. & Zhou, S. Syntrophic growth with direct interspecies electron transfer between pili-free *Geobacter* species. *ISME J.* **12**, 2142–2151 (2018).
38. Zheng, S., Liu, F., Li, M., Xiao, L. & Wang, O. Comparative transcriptomic insights into the mechanisms of electron transfer in *Geobacter* co-cultures with activated carbon and magnetite. *Sci. China Life Sci.* **61**, 787–798 (2018).
39. Aklujkar, M. et al. Proteins involved in electron transfer to Fe(III) and Mn(IV) oxides by *Geobacter sulfurreducens* and *Geobacter uraniireducens*. *Microbiology (Reading)* **159**, 515–535 (2013).
40. Klimes, A. et al. Production of pilus-like filaments in *Geobacter sulfurreducens* in the absence of the type IV pilin protein PilA. *FEMS Microbiol. Lett.* **310**, 62–68 (2010).
41. Richter, L. V., Sandler, S. J. & Weis, R. M. Two isoforms of the *Geobacter sulfurreducens* PilA have distinct roles in pilus biogenesis, cytochrome localization, extracellular electron transfer and biofilm formation. *J. Bacteriol.* **194**, 251–263 (2012).
42. Kim, B.-C. et al. Insights into genes involved in electricity generation in *Geobacter sulfurreducens* via whole genome microarray analysis of the OmcF-deficient mutant. *Bioelectrochemistry* **73**, 70–75 (2008).
43. Cologgi, D. L., Lampa-Pastirk, S., Speers, A. M., Kelly, S. D. & Reguera, G. Extracellular reduction of uranium via *Geobacter* conductive pili as a protective cellular mechanism. *Proc. Natl Acad. Sci. USA* **108**, 15248–15252 (2011).
44. Cologgi, D. L., Otwell, A. E., Speers, A. M., Rotondo, J. A. & Reguera, G. Genetic analysis of electroactive biofilms. *Int. Microbiol.* **24**, 631–648 (2021).
45. Hager, A. J. et al. Type IV pili-mediated secretion modulates *Francisella* virulence. *Mol. Microbiol.* **62**, 227–237 (2006).
46. Kirn, T. J., Bose, N. & Taylor, R. K. Secretion of a soluble colonization factor by the TCP type 4 pilus biogenesis pathway in *Vibrio cholerae*. *Mol. Microbiol.* **49**, 81–92 (2003).
47. Han, X. et al. Twitching motility is essential for virulence in *Dichelobacter nodosus*. *J. Bacteriol.* **190**, 3323–3335 (2008).
48. Oki, H. et al. Interplay of a secreted protein with type IVb pilus for efficient enterotoxigenic *Escherichia coli* colonization. *Proc. Natl Acad. Sci. USA* **115**, 7422–7427 (2018).
49. Kilmury, S. L. N. & Burrows, L. L. Type IV pilins regulate their own expression via direct intramembrane interactions with the sensor kinase PilS. *Proc. Natl Acad. Sci. USA* **113**, 6017–6022 (2016).
50. Tan, Z. et al. The signaling pathway that cGAMP riboswitches found: analysis and application of riboswitches to study cGAMP signaling in *Geobacter sulfurreducens*. *Int. J. Mol. Sci.* **23**, 1183 (2022).
51. Juarez, K. et al. PilR, a transcriptional regulator for pilin and other genes required for Fe(III) reduction in *Geobacter sulfurreducens*. *J. Mol. Microbiol. Biotechnol.* **16**, 146–158 (2009).
52. Hosseinzadeh, P. & Lu, Y. Design and fine-tuning redox potentials of metalloproteins involved in electron transfer in bioenergetics. *Biochim. Biophys. Acta* **1857**, 557–581 (2016).
53. Jumper, J. et al. Highly accurate protein structure prediction with AlphaFold. *Nature* **596**, 583–589 (2021).
54. Hallberg, Z. F. et al. Structure and mechanism of a Hypr GGDEF enzyme that activates cGAMP signaling to control extracellular metal respiration. *eLife* **8**, e43959 (2019).
55. Jimenez Otero, F., Chan, C. H. & Bond, D. R. Identification of different putative outer membrane electron conduits necessary for Fe(III) citrate, Fe(III) oxide, Mn(IV) oxide, or electrode reduction by *Geobacter sulfurreducens*. *J. Bacteriol.* **200**, e00347–18 (2018).
56. Iverson, T. M. et al. Heme packing motifs revealed by the crystal structure of the tetra-heme cytochrome c554 from *Nitrosomonas europaea*. *Nat. Struct. Biol.* **5**, 1005–1012 (1998).
57. Kartal, B. & Keltjens, J. T. Anammox biochemistry: a tale of heme c proteins. *Trends Biochem. Sci.* **41**, 998–1011 (2016).
58. Wang, F. et al. Cryoelectron microscopy reconstructions of the *Pseudomonas aeruginosa* and *Neisseria gonorrhoeae* type IV pili at sub-nanometer resolution. *Structure* **25**, 1423–1435 (2017).
59. Kolappan, S. et al. Structure of the *Neisseria meningitidis* Type IV pilus. *Nat. Commun.* **7**, 13015 (2016).
60. Lovley, D. R. & Walker, D. J. F. *Geobacter* protein nanowires. *Front. Microbiol.* **10**, 2078 (2019).
61. Malvankar, N. S. et al. Structural basis for metallic-like conductivity in microbial nanowires. *mBio* **6**, e00084 (2015).
62. Lovley, D. R. & Holmes, D. E. Electromicrobiology: the ecophysiology of phylogenetically diverse electroactive microorganisms. *Nat. Rev. Microbiol.* **20**, 5–19 (2022).
63. Lovley, D. R. & Yao, J. Intrinsically conductive microbial nanowires for ‘green’ electronics with novel functions. *Trends Biotechnol.* **39**, 940–952 (2021).
64. Lovley, D. R. & Holmes, D. E. Protein nanowires: the electrification of the microbial world and maybe our own. *J. Bacteriol.* **202**, e00331–20 (2020).
65. Bray, M. S. et al. Phylogenetic and structural diversity of aromatically dense pili from environmental metagenomes. *Environ. Microbiol. Rep.* **12**, 49–57 (2020).
66. Craig, L. et al. Type IV pilus structure by cryo-electron microscopy and crystallography: implications for pilus assembly and functions. *Mol. Cell* **23**, 651–662 (2006).
67. Bardiaux, B. et al. Structure and assembly of the enterohemorrhagic *Escherichia coli* type 4 Pilus. *Structure* **27**, 1082–1093 (2019).
68. Lopez-Castilla, A. et al. Structure of the calcium-dependent type 2 secretion pseudopilus. *Nat. Microbiol.* **2**, 1686–1695 (2017).
69. Neuhaus, A. et al. Cryo-electron microscopy reveals two distinct type IV pili assembled by the same bacterium. *Nat. Commun.* **11**, 2231 (2020).
70. Cosert, K. M., Castro-Forero, A., Steidl, R. J., Worden, R. M. & Reguera, G. Bottom-up fabrication of protein nanowires via controlled self-assembly of recombinant *Geobacter* pilins. *mBio* **10**, e02721–19 (2019).
71. Devaraj, A. et al. The extracellular DNA lattice of bacterial biofilms is structurally related to Holliday junction recombination intermediates. *Proc. Natl Acad. Sci. USA* **116**, 25068–25077 (2019).
72. Slinker, J. D., Muren, N. B., Renfrew, S. E. & Barton, J. K. DNA charge transport over 34 nm. *Nat. Chem.* **3**, 228–233 (2011).
73. Butler, J. E., Young, N. D., Aklujkar, M. & Lovley, D. R. Comparative genomic analysis of *Geobacter sulfurreducens* KN400, a strain with enhanced capacity for extracellular electron transfer and electricity production. *BMC Genomics* **13**, 471 (2012).
74. Edwards, M. J., White, G. F., Butt, J. N., Richardson, D. J. & Clarke, T. A. The crystal structure of a biological insulated transmembrane molecular wire. *Cell* **181**, 665–673 (2020).
75. Li, D. B. et al. His/Met heme ligation in the PioA outer membrane cytochrome enabling light-driven extracellular electron transfer by *Rhodospseudomonas palustris* TIE-1. *Nanotechnology* **31**, 354002 (2020).
76. Jiang, X. et al. Which multi-heme protein complex transfers electrons more efficiently? Comparing MtrCAB from *Shewanella* with OmcS from *Geobacter*. *J. Phys. Chem. Lett.* **11**, 9421–9425 (2020).
77. Wang, F. et al. An extensively glycosylated archaeal pilus survives extreme conditions. *Nat. Microbiol.* **4**, 1401–1410 (2019).
78. Huerta-Miranda, G. A., Arroyo-Escoto, A. I., Burgos, X., Juarez, K. & Miranda-Hernandez, M. Influence of the major pilA transcriptional regulator in electrochemical responses of *Geobacter sulfurreducens* PilR-deficient mutant biofilm formed on FTO electrodes. *Bioelectrochemistry* **127**, 145–153 (2019).
79. Malvankar, N. S., Yalcin, S. E., Tuominen, M. T. & Lovley, D. R. Visualization of charge propagation along individual pili proteins using ambient electrostatic force microscopy. *Nat. Nanotechnol.* **9**, 1012–1017 (2014).
80. Ing, N. L., Nusca, T. D. & Hochbaum, A. I. *Geobacter sulfurreducens* pili support ohmic electronic conduction in aqueous solution. *Phys. Chem. Chem. Phys.* **19**, 21791–21799 (2017).
81. De Carlo, S. & Harris, J. R. Negative staining and cryo-negative staining of macromolecules and viruses for TEM. *Micron* **42**, 117–131 (2011).
82. Kemp, A. D., Harding, C. C., Cabral, W. A., Marini, J. C. & Wallace, J. M. Effects of tissue hydration on nanoscale structural morphology and mechanics of individual Type I collagen fibrils in the Brl mouse model of *Osteogenesis imperfecta*. *J. Struct. Biol.* **180**, 428–438 (2012).
83. Jesior, J. C. & Wade, R. H. Electron-irradiation-induced flattening of negatively stained 2D protein crystals. *Ultramicroscopy* **21**, 313–319 (1987).
84. Xu, S. & Arnsdorf, M. F. Scanning (atomic) force microscopy imaging of earthworm haemoglobin calibrated with spherical colloidal gold particles. *J. Microsc.* **187**, 43–53 (1997).
85. Chan, C. H., Levar, C. E., Zacharoff, L., Badalamenti, J. P. & Bond, D. R. Scarless genome editing and stable inducible expression vectors for *Geobacter sulfurreducens*. *Appl. Environ. Microbiol.* **81**, 7178–7186 (2015).
86. Damron, F. H. et al. Construction of mobilizable mini-Tn7 vectors for bioluminescent detection of Gram-negative bacteria and single-copy promoter lux reporter analysis. *Appl. Environ. Microbiol.* **79**, 4149–4153 (2013).
87. Zacharoff, L., Chan, C. H. & Bond, D. R. Reduction of low potential electron acceptors requires the CbcL inner membrane cytochrome of *Geobacter sulfurreducens*. *Bioelectrochemistry* **107**, 7–13 (2016).
88. Marsili, E., Rollefson, J. B., Baron, D. B., Hozalski, R. M. & Bond, D. R. Microbial biofilm voltammetry: direct electrochemical characterization of catalytic electrode-attached biofilms. *Appl. Environ. Microbiol.* **74**, 7329–7337 (2008).
89. Schagger, H. Tricine-SDS-PAGE. *Nat. Protoc.* **1**, 16–22 (2006).

90. Kavran, J. M. & Leahy, D. J. Silver staining of SDS-polyacrylamide gel. *Meth. Enzymol.* **541**, 169–176 (2014).
91. Thomas, P. E., Ryan, D. & Levin, W. An improved staining procedure for the detection of the peroxidase activity of cytochrome P-450 on sodium dodecyl sulfate polyacrylamide gels. *Anal. Biochem.* **75**, 168–176 (1976).
92. Strohal, M., Kavan, D., Novak, P., Volny, M. & Havlicek, V. mMass 3: a cross-platform software environment for precise analysis of mass spectrometric data. *Anal. Chem.* **82**, 4648–4651 (2010).
93. Strohal, M., Hassman, M., Kosata, B. & Kodicek, M. mMass data miner: an open source alternative for mass spectrometric data analysis. *Rapid Commun. Mass Spectrom.* **22**, 905–908 (2008).
94. Niedermeyer, T. H. & Strohal, M. mMass as a software tool for the annotation of cyclic peptide tandem mass spectra. *PLoS ONE* **7**, e44913 (2012).
95. Rohou, A. & Grigorieff, N. CTFIND4: fast and accurate defocus estimation from electron micrographs. *J. Struct. Biol.* **192**, 216–221 (2015).
96. Punjani, A., Rubinstein, J. L., Fleet, D. J. & Brubaker, M. A. cryoSPARC: algorithms for rapid unsupervised cryo-EM structure determination. *Nat. Methods* **14**, 290–296 (2017).
97. Zheng, S. Q. et al. MotionCor2: anisotropic correction of beam-induced motion for improved cryo-electron microscopy. *Nat. Methods* **14**, 331–332 (2017).
98. Egelman, E. H. A robust algorithm for the reconstruction of helical filaments using single-particle methods. *Ultramicroscopy* **85**, 225–234 (2000).
99. Egelman, E. H. Reconstruction of helical filaments and tubes. *Methods Enzymol.* **482**, 167–183 (2010).
100. Afonine, P. V. et al. New tools for the analysis and validation of cryo-EM maps and atomic models. *Acta Crystallogr. D Struct. Biol.* **74**, 814–840 (2018).
101. Pettersen, E. F. et al. UCSF Chimera—a visualization system for exploratory research and analysis. *J. Comput. Chem.* **25**, 1605–1612 (2004).
102. Afonine, P. V. et al. Real-space refinement in PHENIX for cryo-EM and crystallography. *Acta Crystallogr. D Struct. Biol.* **74**, 531–544 (2018).
103. Williams, C. J. et al. MolProbity: more and better reference data for improved all-atom structure validation. *Protein Sci.* **27**, 293–315 (2018).
104. Clarke, T. A., Cole, J. A., Richardson, D. J. & Hemmings, A. M. The crystal structure of the pentahaem c-type cytochrome NrfB and characterization of its solution-state interaction with the pentahaem nitrite reductase NrfA. *Biochem. J.* **406**, 19–30 (2007).
105. Rodrigues, M. L., Oliveira, T. F., Pereira, I. A. & Archer, M. X-ray structure of the membrane-bound cytochrome c quinol dehydrogenase NrfH reveals novel haem coordination. *EMBO J.* **25**, 5951–5960 (2006).
106. Pettersen, E. F. et al. UCSF ChimeraX: structure visualization for researchers, educators, and developers. *Protein Sci.* **30**, 70–82 (2021).

Acknowledgements

Cryo-EM imaging was done at the Molecular Electron Microscopy Core Facility at the University of Virginia, which is supported by the School of Medicine and built with NIH grant no. G20-RR31199. Mass spectrometry was performed in the Department of Chemistry Mass Spectrometry Facility at the University of California, Irvine on an instrument generously donated by Biosera. This work was supported by NIH grant nos. GM122510 (E.H.E.) and K99GM138756 (F.W.), DOE grant no. DE-SC0020322 (A.I.H., D.R.B. and E.H.E.), AFOSR grant no. FA9550-19-1-0380 (A.I.H.), NSF grant no. 2030381 (D.S.), Office of Naval Research grant no. N00014-18-1-2632 (C.H.C., K.J. and S.C.) and the SRCP Seed grant at the University of Washington Bothell (D.S.). We thank B. Katz and C. Wilmot for helpful discussions.

Author contributions

K.M., K.J., C.H.C. and S.C. prepared samples. F.W. performed microscopy, image analysis and model building. V.S., Z.S., D.S. and F.W. carried out analysis of existing multihaem structures. A.I.H., E.H.E. and D.R.B. directed the research. F.W., A.I.H., E.H.E. and D.R.B. wrote the paper.

Competing interests

The authors declare no competing interests.

Additional information

Extended data is available for this paper at <https://doi.org/10.1038/s41564-022-01159-z>.

Supplementary information The online version contains supplementary material available at <https://doi.org/10.1038/s41564-022-01159-z>.

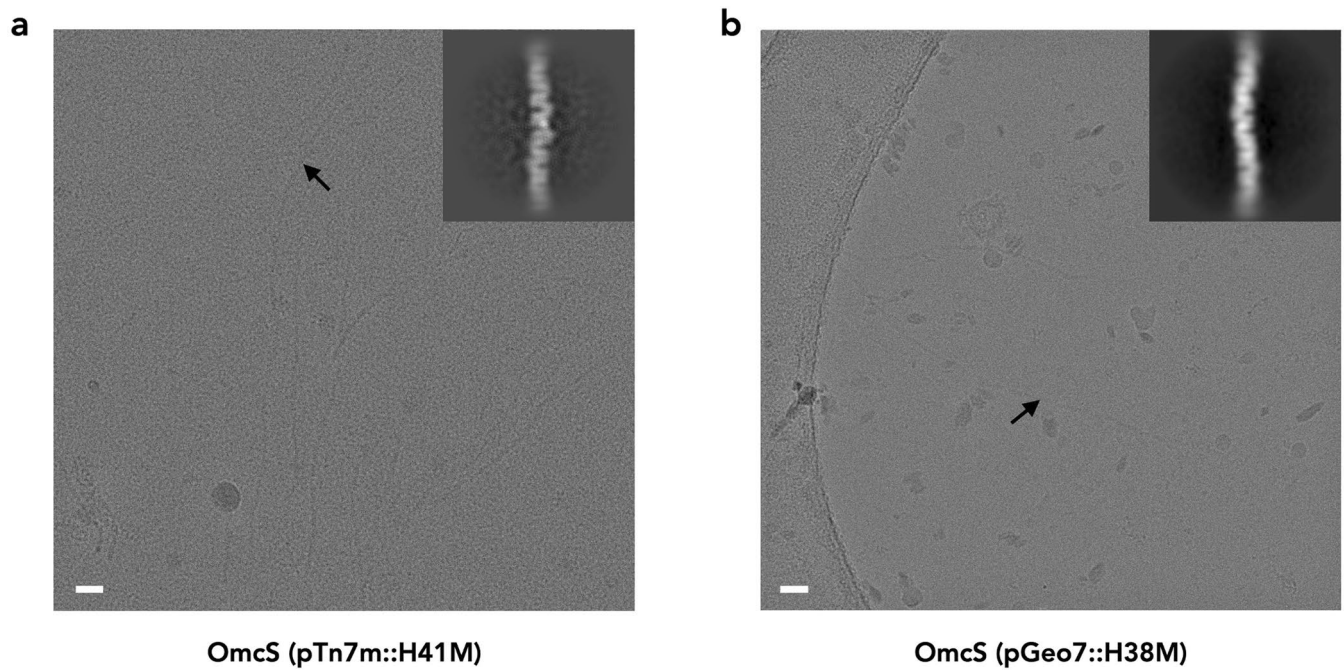
Correspondence and requests for materials should be addressed to Allon I. Hochbaum, Edward H. Egelman or Daniel R. Bond.

Peer review information *Nature Microbiology* thanks Andreas Schramm and the other, anonymous, reviewer(s) for their contribution to the peer review of this work. Peer reviewer reports are available.

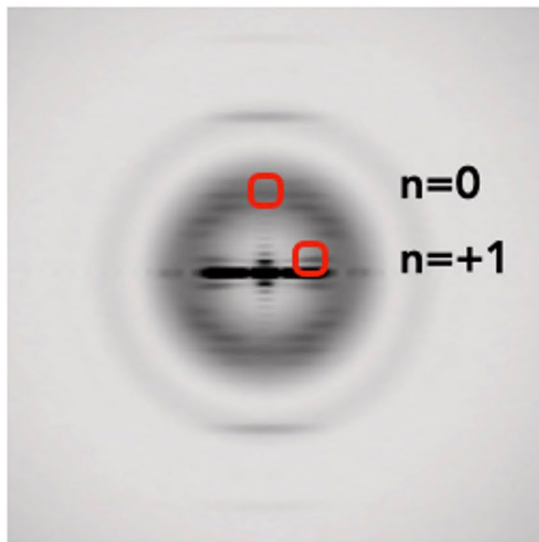
Reprints and permissions information is available at www.nature.com/reprints.

Publisher's note Springer Nature remains neutral with regard to jurisdictional claims in published maps and institutional affiliations.

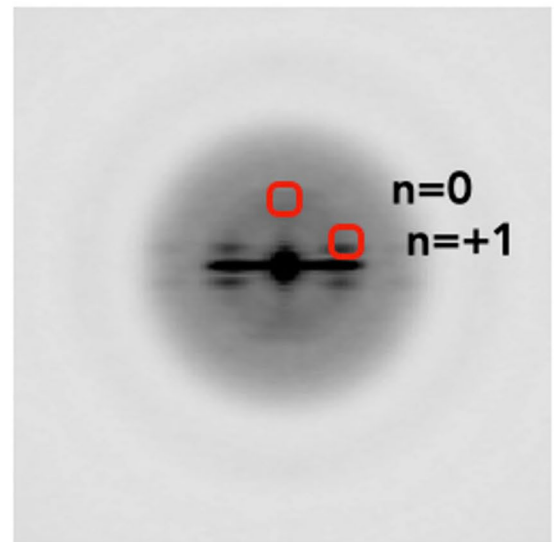
© The Author(s), under exclusive licence to Springer Nature Limited 2022



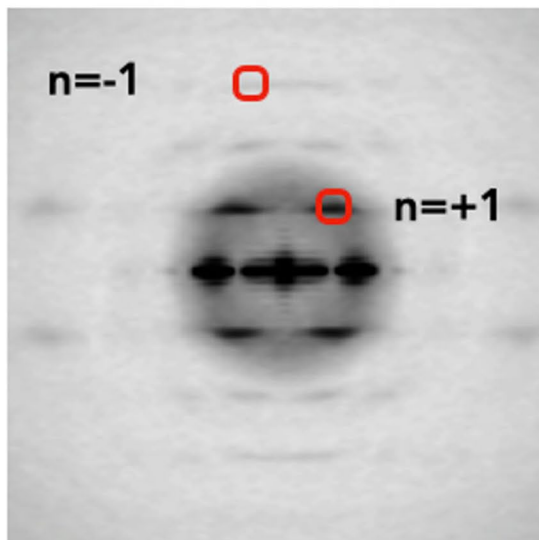
Extended Data Fig. 1 | Cryo-EM images of the purified OmcE filaments. Representative cryo-EM images of the purified OmcE filaments (black arrow) from the pTn7m::OmcS-H41M variant strain (a, from 5,269 images recorded) and pGeo7::OmcS-H38M variant strain (b, from 442 images recorded). The two-dimensional class averages of the OmcE filaments are shown on the top right of each. The sample was treated with DNase I and clarified via centrifugation prior to freezing. Scale bar, 200 Å.



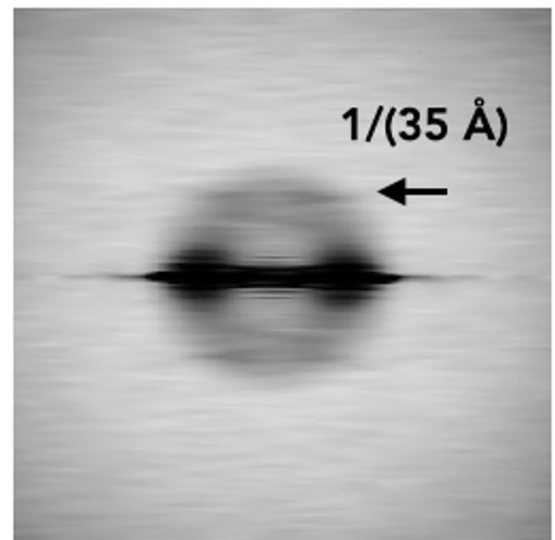
OmcE



OmcS

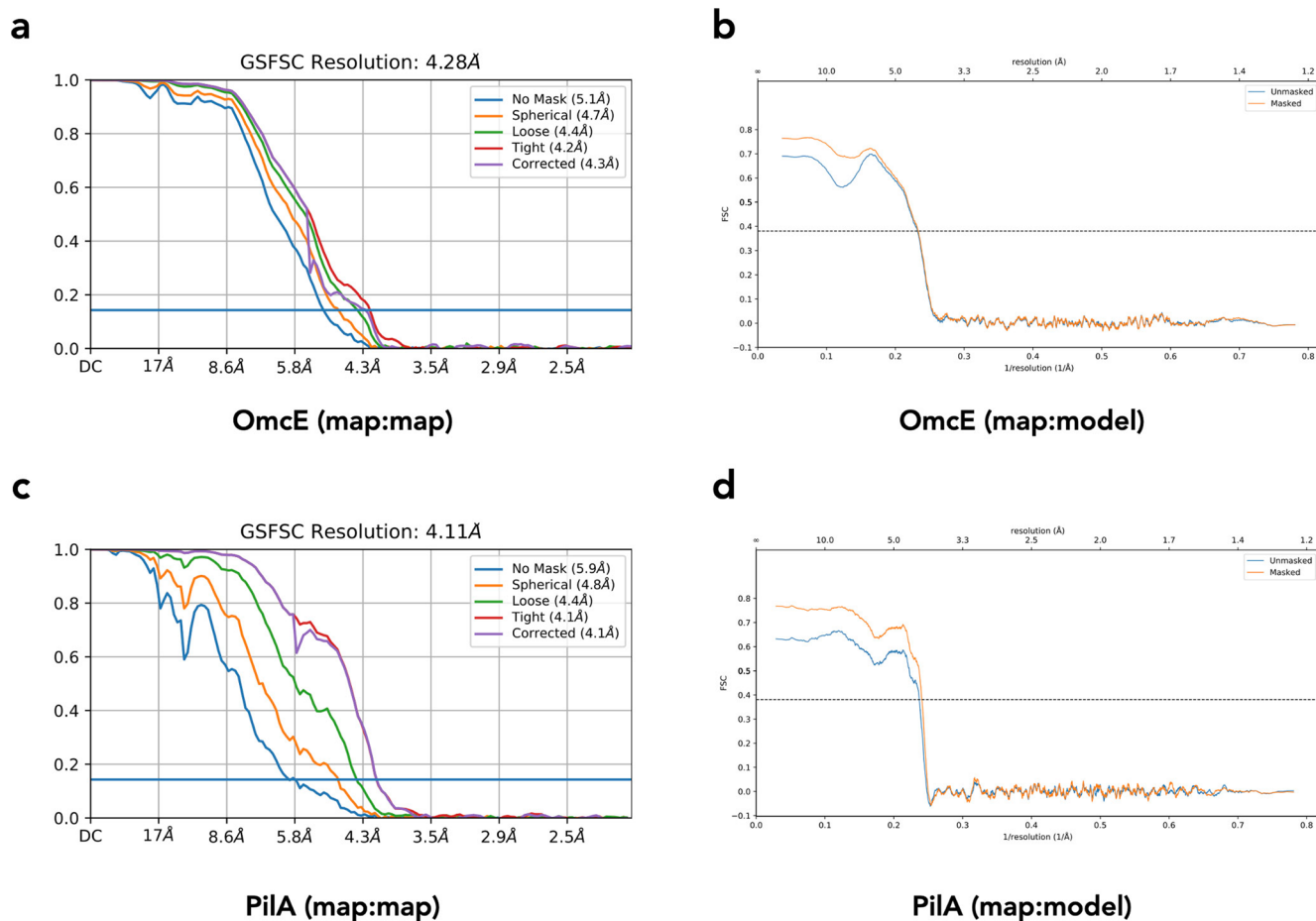


T4P

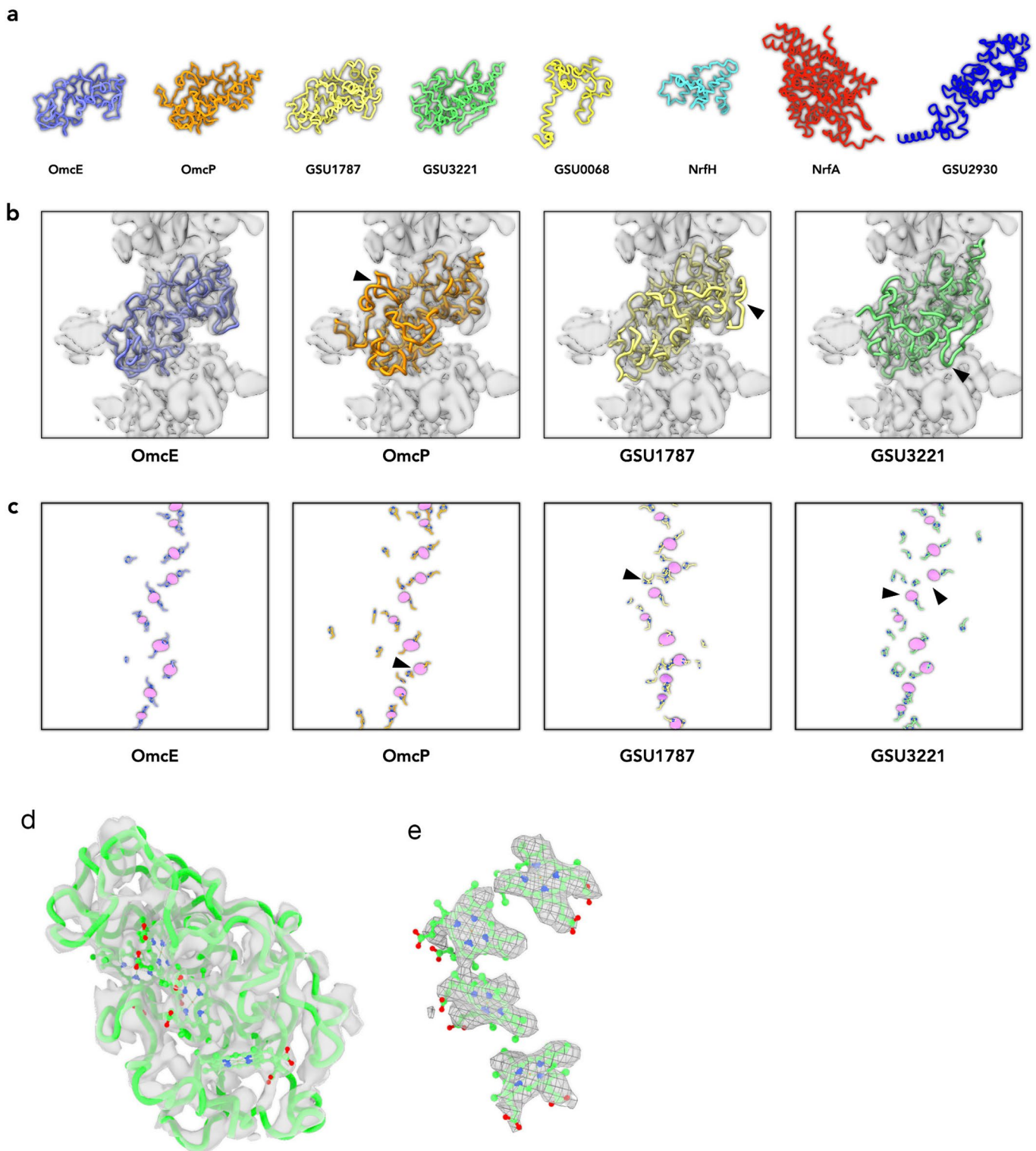


DNA

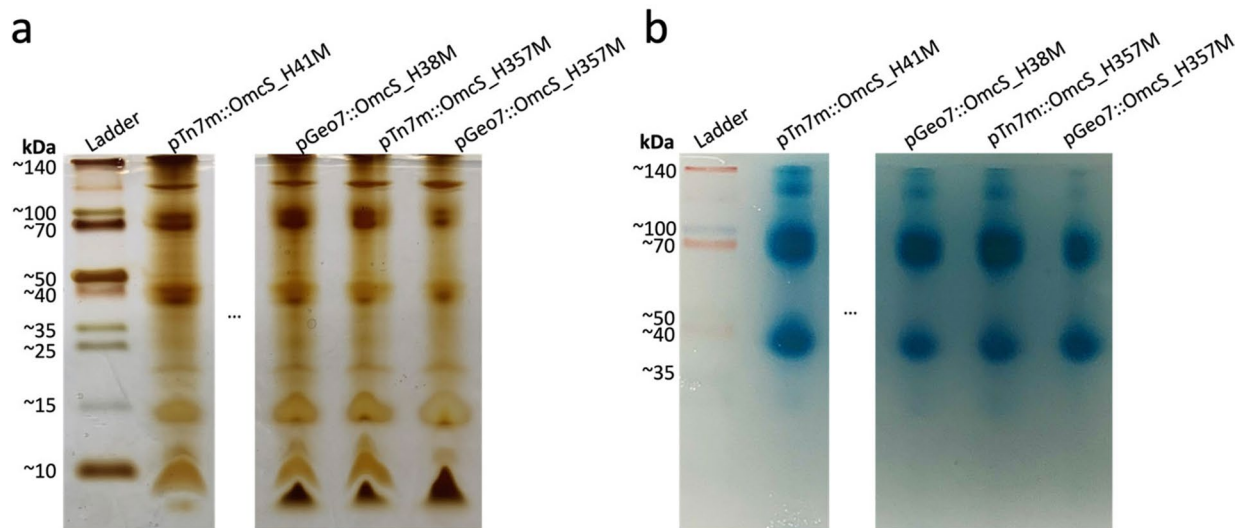
Extended Data Fig. 2 | Averaged power spectra from different filaments. All power spectra were generated from raw images aligned to the same axis.



Extended Data Fig. 3 | Fourier Shell Correlation (FSC) calculations of OmcE and PilA filaments. (a) The map:map FSC calculation of OmcE filament (0.143 cutoff). (b) The model:map FSC calculation of OmcE filament (0.38 cutoff). (c) The map:map FSC calculation of PilA filament (0.143 cutoff). (d) The model:map FSC calculation of PilA filament (0.38 cutoff). The 0.38 threshold is used as it is $\sqrt{0.143}$.

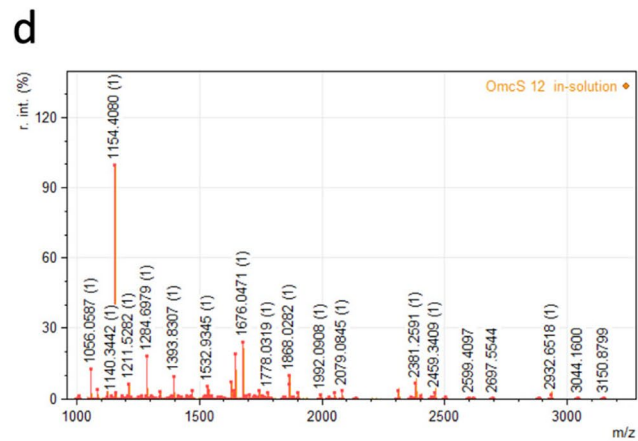


Extended Data Fig. 4 | OmcE is the only good match to the map. (a) AlphaFold2 predictions of eight tetraheme proteins in *Geobacter sulfurreducens*. (b) Docking of a single subunit into the cryo-EM map. The parts not fitting into the map are labeled by black arrowheads. (c) The cryo-EM map was filtered to 6 Å resolution and set to a very high threshold, so the only densities shown (magenta) are the centers of heme molecules. Bis-His coordination of hemes is shown, and only histidines in OmcE coordinate all four hemes. The poorly coordinated hemes are indicated by black arrowheads. (d) The OmcE atomic model fits into the ~4.3 Å cryo-EM map, with protein C α trace and ligand displayed. (e) Fitting of four heme co-factors into the corresponding cryo-EM densities.



C

| Sequence | pTn7m::OmcS H357M |
|----------|-------------------|
| OmcS | 26.4% |
| OmcE | 37.5% |
| GSU1787 | 20.1% |
| GSU2501 | 14.4% |
| GSU3221 | 7.6% |
| OmcP | 0% |
| PilA-N | 58.9% |
| PilA-C | 54.8% |



e Sequence - OmcE

| Accession | Length | Mo. Mass | Av. Mass | Coverage | Matched Int. |
|---|--------|------------|------------|----------|--------------|
| | 232 | 24368.6847 | 24383.9932 | 37.5 % | 7.0 % |
| <p>MRSEVKIGLA LTALLVAVTA AGAASIKNTK HDLSSGSGTGA TFKATNTDQI CVFCHTPHNA QQDIPLWNRG NPTASTFTLY SSSSMNNVPV KQGFTADSI LFCMSCHDGA TGLGGAVHND PNGAAIAMVG GNDLITGEAN LGTDLSNDHP VNFVETPAGI AADGNLGDALD TGTNPPTMKT GDVTNGLPLF KSARGATTLE CGSCHKVHDN TDAPFLRTTM AGSKLCLGCH KK</p> | | | | | |

| Position | Modification | Type | Mo. Mass | Av. Mass | Formula |
|----------|-----------------|----------|----------|----------|--------------|
| All M | Oxidation | variable | 15.9949 | 15.9994 | O |
| All W | Oxidation | variable | 15.9949 | 15.9994 | O |
| All C | Carbamidomethyl | variable | 57.0215 | 57.0514 | CH2CONH2 - H |

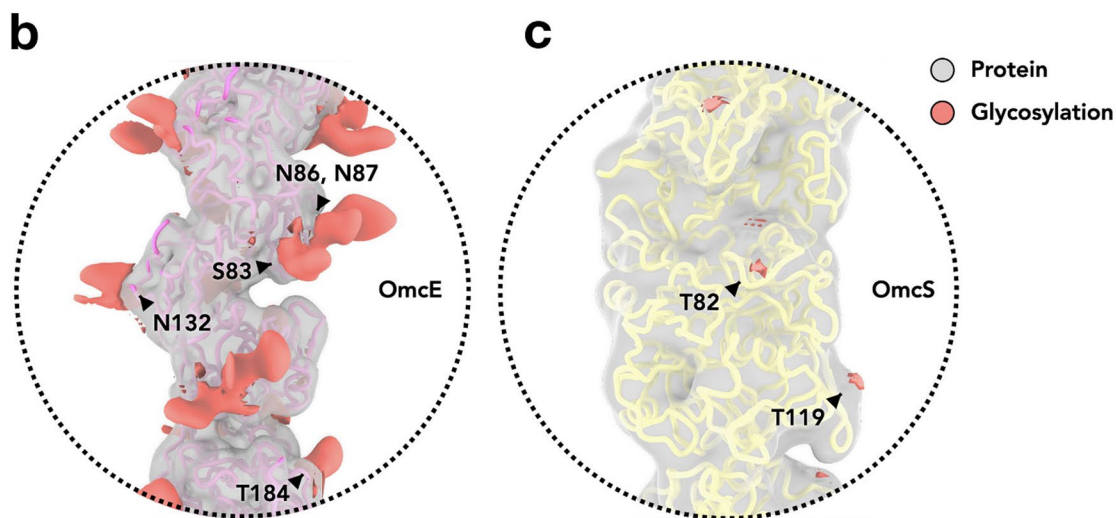
| Meas. m/z | Calc. m/z | δ (Da) | δ (ppm) | Rel. Int. (%) | z | Annotation | Formula |
|-----------|-----------|---------------|----------------|---------------|---|--|-----------------|
| 1261.7072 | 1261.6787 | 0.0285 | 22.6 | 0.86 | 1 | [180-191] k.TGDVTNGLPLFK.s | C57H92N14O18 |
| 1263.6949 | 1263.5456 | 0.1492 | 118.1 | 0.72 | 1 | [195-206] r.GATTLECGSCHK.v [1xCarbamidomethyl] | C49H82N16O19S2 |
| 1284.6979 | 1284.6331 | 0.0648 | 50.4 | 18.01 | 1 | [207-217] k.VHDNTDAPFLR.t | C56H85N17O18 |
| 1307.7332 | 1307.6226 | 0.1106 | 84.6 | 0.75 | 1 | [31-43] k.HDLSSGSGTGATFK.a | C55H86N16O21 |
| 1320.7542 | 1320.5671 | 0.1871 | 141.7 | 0.16 | 1 | [195-206] r.GATTLECGSCHK.v [2xCarbamidomethyl] | C51H85N17O20S2 |
| 1449.8745 | 1449.7011 | 0.1734 | 119.6 | 1.30 | 1 | [218-231] r.TTMAGSKLCLGCHK.k | C59H104N18O18S3 |
| 1522.9473 | 1522.7175 | 0.2298 | 150.9 | 0.76 | 1 | [218-231] r.TTMAGSKLCLGCHK.k [1xCarbamidomethyl]; 1xOxidation] | C61H107N19O20S3 |
| 2367.1766 | 2367.4221 | -0.2455 | -103.7 | 0.27 | 1 | [3-27] r.SEVKIGLALTALLVAVTAAGAASIK.n | C107H191N27O32 |

Extended Data Fig. 5 | See next page for caption.

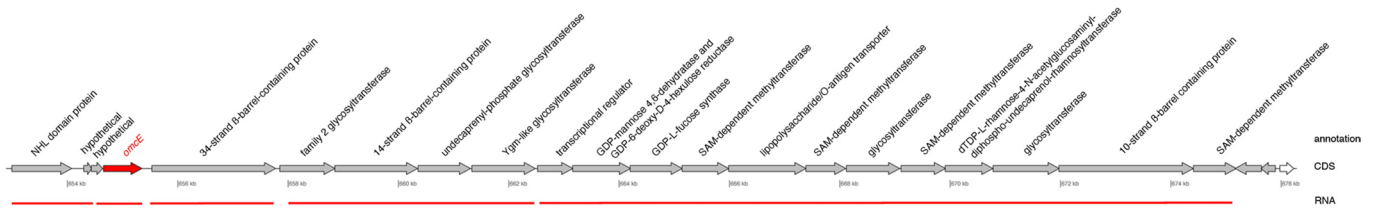
Extended Data Fig. 5 | Mass spectrometry data of isolated filament samples. **(a)** Silver (for protein) and **(b)** 3,3',5,5'- tetramethylbenzidine (for heme) stained SDS-PAGE gels of the four mutants used in this study: pTn7m::OmcS_H41M, pGeo7::OmcS_H38M, pTn7m::OmcS_H357M, pGeo7::OmcS_H357M. Approx. 10 different gels were run during the purification procedure, with the gel shown being the final one. Cryo-EM images of pTn7m::OmcS_H357M were used for OmcE structure determination. OmcE has the highest sequence coverage **(c)** of the four tetraheme cytochromes with similar predicted folds, OmcE, OmcP, GSU1787, GSU3221, from protein sequencing mass spectrometry of in-solution digests of the isolated filament samples. OmcP was not detected in this analysis. **(d)** Mass spectrum and **(e)** sequence matching data of pTn7m::OmcS_H357M filament isolate digest. Underlined sequences are matched peptides from the digest. Red residues are those likely to be chemically modified during sample preparation (see Materials and Methods), as indicated in (e).

a

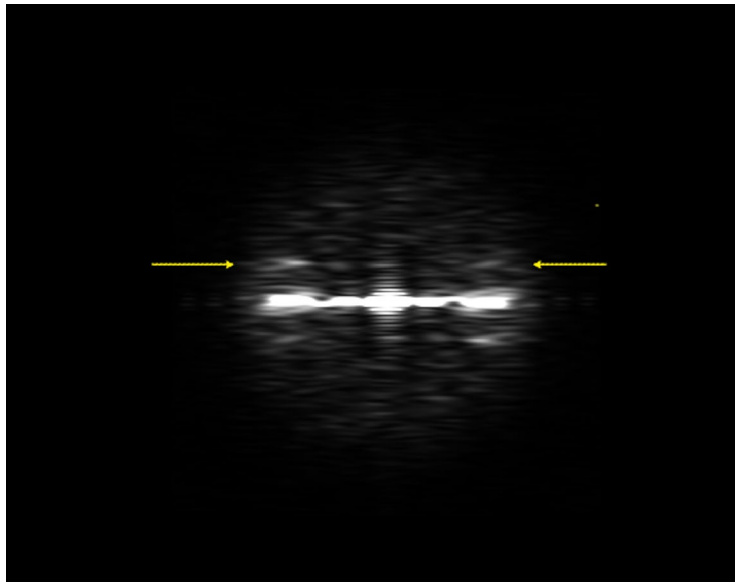
| | | |
|------|--|-----|
| OmcE | 1 MRSEVKIGLALTALLVAVTAAGAASIK----- | 27 |
| OmcS | 1 MKKGMKVSLSVAAAALLMSAPAAFAFHSGGVAECEGCHTMHNSLGGAVMNSATAQFTTGPMLLQGATQSSSCLNCHQHAGDTGPSSYHISTAEAD | 95 |
| OmcE | 28 -----NTKHDLS-----GSTGATFKATNTDQICVFCHTPHNAQQDI----- | 64 |
| OmcS | 96 MPAGTAPLQMTPGGDFGWVKKTYTWNVRGLNTSEGERKGHNI VAGDYNVADTTLTAPGGTYP--ANQLHCSSCHDPHGKYRRFVDGSIATTGL | 188 |
| OmcE | 65 PLWNRGNPTAS-----TFTLYSS-----S-----MNNVP-----VKQGFADSISLFCMSCHDGDATLGGAVHNDPN | 122 |
| OmcS | 189 P KNSGSYQNSNDPTAWGAVGAYRILGGTGYQPKSLSGSYAFANQVPAAVAPSTYNRTEATTQTRVAYGGGMSEWCANCHTDIHNSAYP----- | 277 |
| OmcE | 123 GAAIAMVGGNDLITGEANLGLDLSNDHPVNFVEVTPAGIAADGNLGAALDGTNPPTMKTGDVTN-----GLPLFKSARGAT----- | 197 |
| OmcS | 278 -----TNLRHP-----AGNGAKFGAT AGLYNSYKKSGLD GTQASAYLSLAPFEEGTADYTVLKGHAK DDTA | 341 |
| OmcE | 198 -----TLECGSCHKVHDNTDAPFLRTTM-----AGSKLCLGCHKK----- | 232 |
| OmcS | 342 LTGADATSNVNC SCHRAHASGFDSMTR FNLAYEFTT ADASGNS YGTDPNTSSLQGRSVNEMTAAYYGR TADKFAPYQRALCNKCHAKD | 432 |



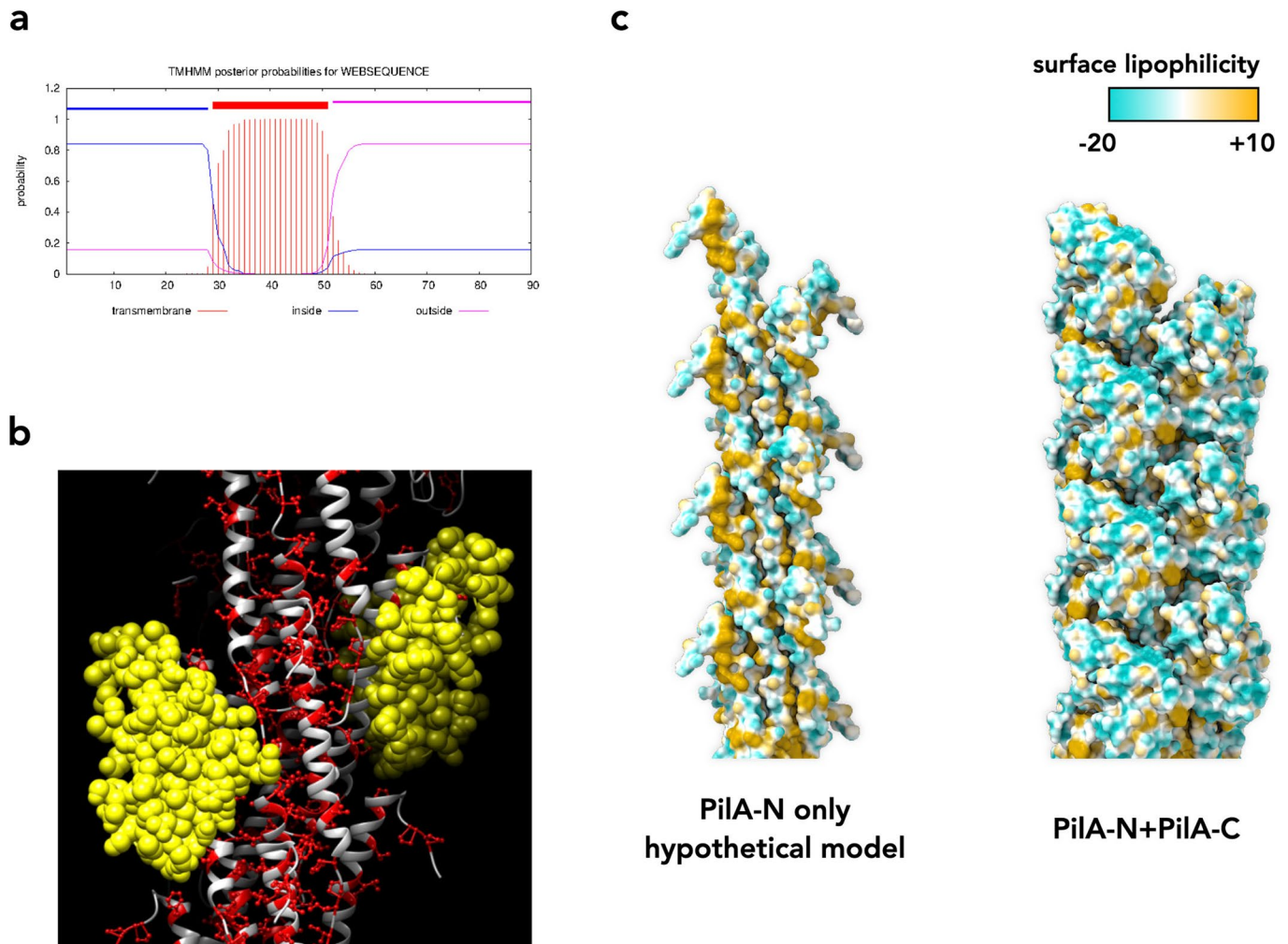
Extended Data Fig. 6 | Comparisons between OmcE and OmcS. (a) All seven histidines in OmcE that coordinate heme molecules within the same subunit are highlighted with red stars. These seven histidines in OmcE have been aligned, based upon the structures, to seven histidines in OmcS, and the order of these residues in the primary sequence is the same in both proteins. The histidine in OmcE that coordinates a heme molecule in an adjacent subunit is labeled with a green star. The structurally aligned histidine in OmcS is marked with a blue star. (b,c) All volumes were filtered to 10 Å for a clear display. The density accounted for by atomic models is colored in gray, and the extra density is colored in red. The backbones of OmcE (a) and OmcS (b) filaments are shown, and they are colored in magenta and yellow, respectively. (b,c) All volumes were filtered to 10 Å for a clear display. The density accounted for by atomic models is colored in gray, and the extra density is colored in red. The backbones of OmcE (b) and OmcS (c) filaments are shown, and they are colored in magenta and yellow, respectively.



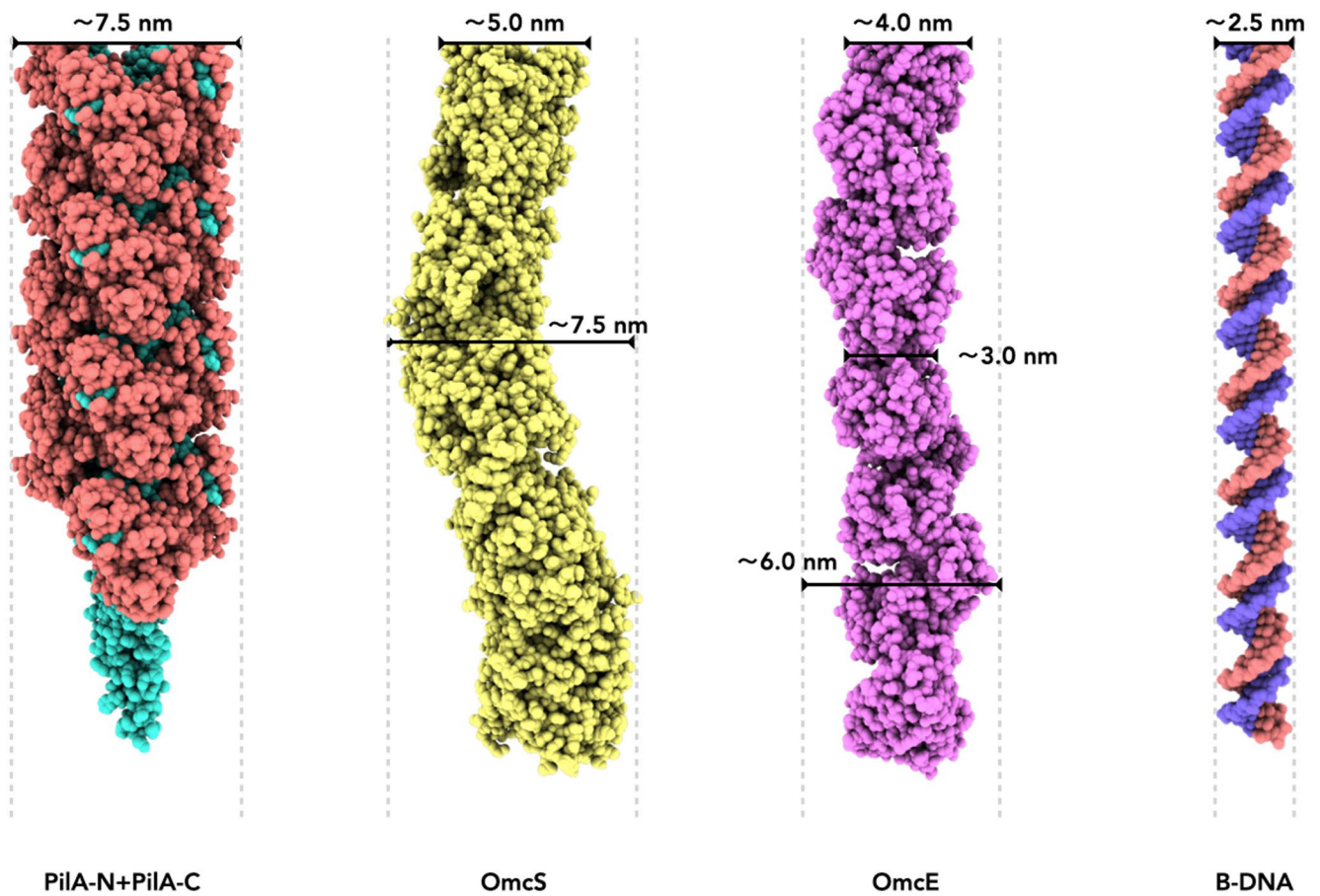
Extended Data Fig. 7 | The *omcE* genomic region. Organization of the *omcE* genomic region, showing the 17-gene cluster downstream containing glycosyltransferases, undecaprenyl-phosphate transferases and sugar modification enzymes. Similar gene clusters exist downstream of all *Geobacter omcE* homologs.



Extended Data Fig. 8 | Analysis of previous images shows OmcS, not PilA, filaments. An averaged power spectrum has been computed from the filaments in Malvankar et al., *mBio* **6**, e00084 (2015), Supplemental Figure S1, labeled 'Transmission electron micrograph of pili of *Geobacter sulfurreducens* strain Aro-5'. The power spectrum shows a periodicity of $\sim 1/(200 \text{ \AA})$ marked by the yellow arrows, indicating that these filaments are actually composed of the cytochrome OmcS and are not pili.



Extended Data Fig. 9 | PilA-N chain is highly hydrophobic. (a) Transmembrane predictions of PilA-N by TMHMM2. The first ~25 residues are predicted to be signal peptide and would be cleaved in the mature protein. (b) PilA-C domains bury hydrophobic surface of PilA-N. The hydrophobic residues (Val, Leu, Ile, Met, Phe, Pro and Try) in PilA-N are shown in ball and stick representation in red. The outer globular domain (PilA-C) is shown in yellow for two neighboring subunits. It can be seen that these N-terminal hydrophobic residues get buried by the C-terminal chain when the filament is formed, suggesting that a filament composed of only PilA-N would contain too many surface-exposed hydrophobic residues to be soluble. (c) The hydrophobicity (or lipophilicity) can be compared between a model for a PilA-N only filament (left) and the observed PilA-N/C filament (right). The rather hydrophobic surface for the PilA-N model suggests that it might not be soluble.



Extended Data Fig. 10 | Diameter estimations of four different filaments from atomic models. The atomic models without hydrogens are shown with atoms represented by spheres having the appropriate van der Waals radii.

Reporting Summary

Nature Portfolio wishes to improve the reproducibility of the work that we publish. This form provides structure for consistency and transparency in reporting. For further information on Nature Portfolio policies, see our [Editorial Policies](#) and the [Editorial Policy Checklist](#).

Statistics

For all statistical analyses, confirm that the following items are present in the figure legend, table legend, main text, or Methods section.

n/a Confirmed

- The exact sample size (n) for each experimental group/condition, given as a discrete number and unit of measurement
- A statement on whether measurements were taken from distinct samples or whether the same sample was measured repeatedly
- The statistical test(s) used AND whether they are one- or two-sided
Only common tests should be described solely by name; describe more complex techniques in the Methods section.
- A description of all covariates tested
- A description of any assumptions or corrections, such as tests of normality and adjustment for multiple comparisons
- A full description of the statistical parameters including central tendency (e.g. means) or other basic estimates (e.g. regression coefficient) AND variation (e.g. standard deviation) or associated estimates of uncertainty (e.g. confidence intervals)
- For null hypothesis testing, the test statistic (e.g. F , t , r) with confidence intervals, effect sizes, degrees of freedom and P value noted
Give P values as exact values whenever suitable.
- For Bayesian analysis, information on the choice of priors and Markov chain Monte Carlo settings
- For hierarchical and complex designs, identification of the appropriate level for tests and full reporting of outcomes
- Estimates of effect sizes (e.g. Cohen's d , Pearson's r), indicating how they were calculated

Our web collection on [statistics for biologists](#) contains articles on many of the points above.

Software and code

Policy information about [availability of computer code](#)

Data collection

Data analysis

For manuscripts utilizing custom algorithms or software that are central to the research but not yet described in published literature, software must be made available to editors and reviewers. We strongly encourage code deposition in a community repository (e.g. GitHub). See the Nature Portfolio [guidelines for submitting code & software](#) for further information.

Data

Policy information about [availability of data](#)

All manuscripts must include a [data availability statement](#). This statement should provide the following information, where applicable:

- Accession codes, unique identifiers, or web links for publicly available datasets
- A description of any restrictions on data availability
- For clinical datasets or third party data, please ensure that the statement adheres to our [policy](#)

The three-dimensional reconstruction for OmcE has been deposited in the Electron Microscopy Data Bank with accession code EMD-25879 (<https://www.ebi.ac.uk/emdb/EMD-25879>), and the atomic model has been deposited in the Protein Data Bank with accession code 7TFS (<https://www.rcsb.org/structure/7Tfs>). The three-dimensional reconstruction for PiLA-N/C has been deposited in the Electron Microscopy Data Bank with accession code EMD-25881 (<https://www.ebi.ac.uk/emdb/EMD-25881>), and the atomic model has been deposited in the Protein Data Bank with accession code 7TGG (<https://www.rcsb.org/structure/7Tgg>). Other atomic models used in the study were PDB 2P0B (<https://www.rcsb.org/structure/2p0b>), 2J7A (<https://www.rcsb.org/structure/2j7a>) and 6VK9 (<https://www.rcsb.org/structure/6vk9>).

Field-specific reporting

Please select the one below that is the best fit for your research. If you are not sure, read the appropriate sections before making your selection.

Life sciences Behavioural & social sciences Ecological, evolutionary & environmental sciences

For a reference copy of the document with all sections, see [nature.com/documents/nr-reporting-summary-flat.pdf](https://www.nature.com/documents/nr-reporting-summary-flat.pdf)

Life sciences study design

All studies must disclose on these points even when the disclosure is negative.

| | |
|-----------------|--|
| Sample size | <input type="text" value="Described"/> |
| Data exclusions | <input type="text" value="No data were excluded"/> |
| Replication | <input type="text" value="Described"/> |
| Randomization | <input type="text" value="Not relevant."/> |
| Blinding | <input type="text" value="Not relevant."/> |

Reporting for specific materials, systems and methods

We require information from authors about some types of materials, experimental systems and methods used in many studies. Here, indicate whether each material, system or method listed is relevant to your study. If you are not sure if a list item applies to your research, read the appropriate section before selecting a response.

Materials & experimental systems

Methods

- | n/a | Involvement in the study |
|-------------------------------------|--|
| <input checked="" type="checkbox"/> | <input type="checkbox"/> Antibodies |
| <input checked="" type="checkbox"/> | <input type="checkbox"/> Eukaryotic cell lines |
| <input checked="" type="checkbox"/> | <input type="checkbox"/> Palaeontology and archaeology |
| <input checked="" type="checkbox"/> | <input type="checkbox"/> Animals and other organisms |
| <input checked="" type="checkbox"/> | <input type="checkbox"/> Human research participants |
| <input checked="" type="checkbox"/> | <input type="checkbox"/> Clinical data |
| <input checked="" type="checkbox"/> | <input type="checkbox"/> Dual use research of concern |

- | n/a | Involvement in the study |
|-------------------------------------|---|
| <input checked="" type="checkbox"/> | <input type="checkbox"/> ChIP-seq |
| <input checked="" type="checkbox"/> | <input type="checkbox"/> Flow cytometry |
| <input checked="" type="checkbox"/> | <input type="checkbox"/> MRI-based neuroimaging |